Journal of Catalysis 266 (2009) 129–144

Contents lists available at ScienceDirect

Journal of Catalysis

journal homepage: www.elsevier.com/locate/jcat

Cobalt particle size effects in Fischer–Tropsch synthesis: structural and *in situ* spectroscopic characterisation on reverse micelle-synthesised Co/ITQ-2 model catalysts

Gonzalo Prieto [a], Agustín Martínez [a,*], Patricia Concepción [a], Ramón Moreno-Tost [b]

[a] Instituto de Tecnología Química, UPV-CSIC, Avda. de los Naranjos s/n, 46022 Valencia, Spain
[b] Universidad de Málaga, Facultad de Ciencias, Departamento de Química Inorgánica, Cristalografía y Mineralogía, Unidad Asociada al ICP-CSIC, Campus de Teatinos, 29071 Málaga, Spain

ARTICLE INFO

Article history:
Received 27 March 2009
Revised 27 May 2009
Accepted 1 June 2009
Available online 5 July 2009

Keywords:
Fischer–Tropsch
Co/ITQ-2
Model catalysts
Particle size effects
At work CO-FTIR
Metal surface reconstruction

ABSTRACT

A series of 10%Co/ITQ-2 model catalysts have been prepared by combining a reverse micellar synthesis with a surface silylated ITQ-2 delaminated zeolite. The catalysts display rather uniform Co^0 particle size distributions in the 5–11 nm range as ascertained by XRD, H_2-chemisorption and (HR)TEM. Additionally, a low dispersed 30%Co/SiO_2 reference sample ($d(Co^0)$ = 141 nm) has been prepared by supporting a Co_3O_4 nanopowder on spherical SiO_2. H_2-TPR and DR UV–vis spectroscopy reveal that the preparative approach leads to highly reducible catalysts in the $d(Co^0)$ range of 5.6–141 nm, while the activation energies for the stepwise $Co_3O_4 \rightarrow CoO \rightarrow Co^0$ reduction are found to be particle size dependent. Formation of barely reducible surface and bulk Co silicate species is observed for samples with $d(Co_3O_4) \leqslant 5.9$ nm. Under realistic Fischer–Tropsch synthesis conditions (493 K, 2.0 MPa) the TOF increases from 1.2×10^{-3} to 8.6×10^{-3} s^{-1} when $d(Co^0)$ is increased from 5.6 to 10.4 nm, and then it remains constant up to a particle size of 141 nm. *In situ* and *at work* FTIR of adsorbed CO reveal a severe cobalt surface reconstruction towards more open crystal planes and/or defect sites (Co–carbonyl bands in the region of 2000–2025 cm^{-1}) and suggest adsorbed C adatoms (surface carbidic species), derived from CO dissociation, as the true restructuring agent. Under FTS conditions, this Co surface reconstruction occurs similarly irrespective of the metal particle size. Moreover, an enhancement in the proportion of Co–SiO_2 interfacial $Co^{\delta+}$ sites (Co–CO band at 2060 cm^{-1}) takes place particularly in small cobalt nanoparticles (5.6 nm) likely as a consequence of nanoparticle flattening, as suggested by TEM after catalysis. These Co–SiO_2 interfacial sites are tentatively proposed as responsible for the decreased TOF observed for $d(Co^0) < 10$ nm.

1. Introduction

The Fischer–Tropsch synthesis (FTS) is at the core of the gas-to-liquids (GTLs) processes which have recently received a renewed interest as a versatile catalytic route for producing high quality ultra-clean fuels from synthesis gas or *syngas* ($CO + H_2$) [1]. This interest is mainly driven by the increasingly stringent environmental legislation on transportation fuels and the possibility to monetise abundant and remote natural gas reserves as well as renewable biomass sources with independence from the petroleum supply [2]. Of particular interest is the Fischer–Tropsch-derived (or *synthetic*) diesel fuel, which displays substantially higher cetane number (typically above 70) than that obtained in conventional refineries from crude oil while being virtually free of environmentally harmful sulphur. Cobalt-based catalysts are preferentially applied in FTS processes aimed at producing precursors of the synthetic diesel owing to their high selectivity towards long chain *n*-paraffins, their remarkable stability and their lower activity for the competing water gas shift reaction (WGSR) as compared to alternative catalysts based on iron [3].

As metallic Co^0 sites are the active species in FTS, an intense effort has been devoted to prepare novel catalysts with improved metal dispersion as a reasonable strategy enhance the amount of exposed metallic cobalt atoms. In this sense, preparative routes such as homogeneous deposition–precipitation [4], electrostatic adsorption of Co complexes [5] or mixed sol–gel procedures [6] have been applied to prepare Co-based catalysts with improved metal dispersion. In addition, the use of catalytic supports having advanced textures such as ordered mesoporous silicas [7–9], delaminated zeolites [10], high surface area carbon [11] or nanofibrous inorganic materials [12] and the optimisation of the thermal history during activation of the precursor materials [13] have allowed to prepare FTS catalysts comprising very small cobalt

* Corresponding author. Fax: +34 963877808.
E-mail address: amart@itq.upv.es (A. Martínez).

0021-9517/$ - see front matter © 2009 Elsevier Inc. All rights reserved.
doi:10.1016/j.jcat.2009.06.001

nanoparticles. Nevertheless, in most cases the original expectation of an improved catalytic activity in highly dispersed Co catalysts has turned into unexpectedly low reaction rates as well as decreased selectivities to the desired long-chain hydrocarbons [7,9,10]. This decreased catalytic activity and selectivity towards heavy products have been traditionally ascribed to the existence of unreduced Co species after the reductive pre-treatments, as a consequence of the much lower reducibility displayed by very small Co nanoparticles when supported on typical inorganic carriers (SiO_2, Al_2O_3 or TiO_2) [9,14,15]. Other authors, however, claimed a cobalt particle size effect as responsible for the lower intrinsic (per Co^0 site) catalytic activity (usually expressed as *turnover frequency* or TOF) observed in highly dispersed catalysts [16–19], although the possibility of a certain disguise due to the presence of unreduced Co species could not be ruled out in the majority of the cases [16,17]. Contrary, dissenting results reporting the absence of a clear correlation between particle size and the intrinsic catalytic activity can also be found [20–22].

Thus, the true influence of cobalt particle size has been a long-lasting debate in the FTS literature. It is widely accepted, as shown by Iglesia and co-workers [21], that the intrinsic site reaction rate does not depend on the Co particle size in the range of ca. 10–200 nm where highly reducible catalysts can be obtained by conventional preparations, such as impregnation. Recently, Bezemer et al. [19] succeeded in studying the effect of particle size on the catalytic rate by using Co catalysts supported on inert carbon nanofibres (Co/CNFs) which can be completely reduced, using standard procedures, while displaying metal particle sizes in the elusive range of 3–10 nm. Their results pointed to a *non-classical structure sensitivity* where TOF continuously increases with increasing metal particle size up to an optimum $d(Co^0)$ of 6–8 nm and remains invariant for larger particles. This behaviour differs from the *classical structure sensitivity* which is related to the metal surface crystallographic anisotropy and becomes apparent only when the particle size is reduced typically below 3–4 nm [23]. A particle size-dependent metal surface reconstruction during the Fischer–Tropsch reaction has been proposed as a suitable explanation on the basis of the reported ability of CO to reorganise metallic surfaces and the experimental EXAFS results showing a decrease in the mean Co coordination number under FTS conditions [19]. Thus, the particle size effects have been tentatively connected to structural changes suffered by the catalyst when exposed to *syngas* under FTS conditions.

Many recent studies have contributed with valuable knowledge on the elucidation of the preferred structure of the metallic sites for CO adsorption and reaction [24,25] and the chemical modifications, such as re-oxidation due to the high water partial pressure [26,27], as well as on the structural changes, such as an adsorbate-induced surface reconstruction [28–30], experienced by cobalt in the course of FTS. Nevertheless, since most of these studies are based on DFT theoretical calculations [25,30] or employ single-crystal foils in the *operando* spectroscopic experiments [28,29], some difficulties arise to link their results with other experimental facts that seem to be exclusive of real supported Co catalysts, such as the particle size influence on the intrinsic activity and selectivity. The overcoming of this "*materials gap*" prompts to the use of novel model catalysts which should combine controlled and well-defined features (i.e. metal dispersion, reducibility) with a nature as close as possible to the realistic catalytic systems (as those employed in the GTL processes). The *in situ* characterisation of these model catalysts under certain modelling conditions or "*at work*" during realistic catalytic experiments is expected to provide insight on the cause for the experimentally observed particle size-dependent activity and selectivity in the Co-catalysed FTS.

In this sense, we recently reported the preparation of nearly monodispersed Co/ITQ-2 catalysts by combining an *ex*-support control of the metal dispersion using reverse micelles with a surface-silylated delaminated ITQ-2 zeolite. This methodology allows for an enhanced reducibility for Co nanoparticles of only 4–5 nm in size, at industrially relevant metal loadings (10 wt%) [31]. Preliminary results presented in that work showed a marked decrease in TOF for very small Co nanoparticles (4–5 nm), as compared to larger particles (>10 nm), in spite of their high reducibility. In the present work, this approach is extended to prepare model Co/ITQ-2 catalysts with narrow particle size distributions in the range <10 nm where the size-dependent intrinsic activity has been shown to occur. The model catalysts are structurally characterised to gain insight on all their features that are size dependent, and evaluated in the FTS under realistic conditions. Finally, *in situ* and *operando* characterisation by FTIR of adsorbed CO are performed to evaluate the occurrence of structural changes upon exposure to CO or *syngas* and their consequences in connection with the size-dependent activity are discussed.

2. Experimental

2.1. Preparation of catalysts

2.1.1. Synthesis of delaminated ITQ-2 zeolite

All silica delaminated ITQ-2 zeolite was synthesised following the procedure developed at the ITQ and reported elsewhere [32]. In brief, the interlaminar space of a layered zeolite precursor having MWW structure was swelled by dispersing it in an aqueous solution of cetyltrimethylammonium bromide (CTABr, 29 wt%) and tetrapropylammonium hydroxide (TPAOH, 40 wt%) under reflux conditions for 16 h. The zeolitic layers were afterwards forced apart by sonication (50 W, 40 kHz) for 1 h and the solid recovered by centrifugation after the pH was lowered to 2 by addition of HCl(aq). The obtained solid was then calcined in flowing air at 823 K for 5 h to remove the organic material.

2.1.2. Surface silylation of ITQ-2

The surface silylation of the siliceous support has been shown to be crucial in attaining high reducibilities for highly dispersed catalysts due to the protective role of the surface organic capping, avoiding reaction of Co^{2+} against the surface silanol groups during the decomposition of Co precursors [31]. The calcined ITQ-2 was degassed at 573 K for 2 h and suspended under protective N_2 atmosphere in a solution of 1,1,1,3,3,3-hexamethyldisilazane (HMDS) as silylating agent in toluene having the molar ratios 1 ITQ-2 (SiO_2): 0.15 HMDS: 10 toluene. The suspension was refluxed under flowing N_2 and then filtered, washed extensively with toluene and dried at room temperature overnight [33]. To completely remove the excess of organic moieties, the silylated ITQ-2 was further refluxed in excess ethanol overnight, filtered, washed with ethanol and dried at 373 K. The silylated ITQ-2 support is denoted as S/ITQ-2 along the work.

2.1.3. Incorporation of cobalt

Cobalt nanoparticles were synthesised in a reverse micellar medium following the previously reported procedure [31] with some modifications. In the present case, to extend the range for the metal particle size, a double microemulsion system has been used. A first reverse microemulsion was prepared by dissolving the non-ionic surfactant Triton X114 ((1,1,3,3-Tetramethylbutyl)phenyl-polyethylene glycol, Aldrich) in cyclohexane (Scharlau Chimie, reagent grade). The concentration in surfactant has been varied in the range 0.06–1.3 M. Then, 2-propanol (Aldrich, 99.5%) was added as a modifier of the organic phase in a 2-propanol/cyclohexane molar ratio of 1.7. The organic solution was stirred at room temperature while displacing the air by an Ar flow. An

aqueous solution of $Co(NO_3)_2{\cdot}6H_2O$ (Aldrich) was then added to the organic solution of the surfactant to generate a pink-coloured transparent microemulsion. The cobalt concentration in the aqueous solution was also varied in the range 0.05–3.0 M.

Additionally, a twin reverse microemulsion was prepared in the same way containing hydrazine ($N_2H_4{\cdot}H_2O$, 98% Aldrich) as reductive reagent in the aqueous phase instead of cobalt. The amount of hydrazine used was set to 8, 10 or 16 folds (see Table 1) that required to ideally completely reduce the cobalt species according to the stoichiometry given by Eq. (1)

$$2Co^{2+} + N_2H_4 + 4OH^- \rightarrow 2Co + N_2 + 4H_2O. \quad (1)$$

The hydrazine-bearing microemulsion was added to the cobalt containing microemulsion under sweeping Ar. A light brown suspension appeared whose colour shade depends on the microemulsion parameters as an indication of different sizes of particles growing in the reverse micellar medium. It should be remarked that hydrazine is not able to reduce Co^{2+} ions to Co^0 at room temperature and, indeed, a hydroxi-hydrazine complex is formed [34,35]. Nevertheless, nucleation and growth of this complex is influenced by the parameters of the microemulsion (Table 1) and thus size control on the final Co particle can be effected through this preparative route. The suspension was stirred under Ar for 3 min and then the support (S/ITQ-2) added and the suspension sonicated under Ar for 1 min to properly disperse the support nanosheets. The amount of support was set to yield a 10 wt% cobalt loading in the catalysts. Afterwards, tetrahydrofurane (HPLC grade, Aldrich) was added dropwise under flowing Ar to ensure a complete destabilisation of the micelles and deposition of cobalt–hydrazine complexes on the support. The solid was then filtered, washed exhaustively with *n*-heptane and ethanol, and dried at room temperature overnight. Finally, the catalyst was calcined by slowly heating the sample (1 K/min) from room temperature to 773 K in flowing diluted air (air:N_2 = 1:1 vol/vol) to allow for a slow decomposition of the Co precursors and crystallisation of Co oxides. Then, the flowing gas was switched to pure air and the temperature maintained at 773 K for three additional hours in order to remove the remaining surfactant and the anchored trimethylsilyl groups. Calcination of the catalysts is performed aiming at both crystallising Co as Co_3O_4 and removing the organic surface groups thus leading to model oxide supported Co catalysts that would be more representative of industrial Co-based FTS catalysts. Model Co/ITQ-2 catalysts have been denoted as 10%Co/ITQ(x), where x = 1–7 depending on the microemulsion employed in their preparation, as collected in Table 1.

An additional low-dispersed model catalyst has been prepared by supporting commercial nanosized Co_3O_4 (Aldrich) on a porous SiO_2 (Silica-gel 100, Fluka). The Co_3O_4 nanopowder was co-suspended in ethanol with the required amount of the silica carrier to yield 30 wt% Co loading and the suspension was sonicated for 30 min. The solvent was then removed in a rotary evaporator and the solid finally dried and air-calcined as previously described for Co/ITQ-2 catalysts. The metal loading has been set to 30% in this catalyst (sample named as 30%Co/SiO_2) aiming at attaining the desired CO conversion level (~10%) within the range of experimental conditions allowed by the reactor volume and gas-flow meters during the catalytic experiments.

Table 1
Details of the reverse microemulsion parameters and the reductant amount employed to prepare the Co/ITQ-2 model catalysts.

Catalyst	R (mol/mol)[a]	$[Co]_{aq}$[b] (mol/L)	$[Surf]_{org}$[c] (mol/L)	Red.[d] Excess
10%Co/ITQ(1)	50	3.0	0.06	8
10%Co/ITQ(2)	25	1.65	0.13	8
10%Co/ITQ(3)	10	0.56	0.65	8
10%Co/ITQ(4)	7	0.30	0.65	8
10%Co/ITQ(5)	5	0.24	0.65	8
10%Co/ITQ(6)	5	0.10	0.80	10
10%Co/ITQ(7)	5	0.05	1.30	16

[a] R: water-to-surfactant molar ratio.
[b] Cobalt molar concentration in the aqueous phase.
[c] Surfactant concentration in the organic solvent.
[d] Number of times hydrazine is in excess with respect to the stoichiometric amount according to (Eq. (1)) (see text).

2.2. Characterisation techniques

The amount of Co in the calcined catalysts was determined by ICP-OES in a Varian 715-ES spectrometer after complete dissolution of the solids (ca. 20 mg) in a HNO_3/HF/HCl solution (1/1/3 volume ratio). Elemental analysis was also performed in a Fisons EA1108 instrument using sulphanilamide as standard to determine the carbon content in the catalytic supports and the calcined catalysts.

The N_2 adsorption–desorption isotherms for the ITQ-2 and commercial SiO_2 supports were measured in a Micromeritics ASAP 2000 equipment. The samples (ca. 200 mg) were degassed at 673 K (pristine ITQ-2 and commercial SiO_2) and at 473 K (S/ITQ-2) for 24 h prior to analysis. Specific surface areas were estimated by using the B.E.T. approach. Pore size distributions were obtained by applying the B.J.H. formalism to the adsorption branch of the isotherms.

X-ray diffraction patterns were acquired at room temperature in a Phillips X'pert diffractometer using monochromatised CuK_α radiation. The average particle size of Co_3O_4 in the calcined catalysts was estimated from the Scherrer's equation applied to the most intense (3 1 1) diffraction (2θ = 36.9°) using a shape factor K = 0.9. The FWHM of the peak was determined after Gaussian fitting using the Philips APDW software and quartz (Merck) for determination of the instrumental broadening. The mean Co^0 particle size in reduced catalysts ($d(Co^0)_x$, where the suffix X denotes XRD) was then obtained from the corresponding Co_3O_4 particle size by applying the molar volume correction [36]: $d(Co^0)_x = 3/4d(Co_3O_4)$.

Diffuse reflectance (DR) UV–vis spectra were collected at room temperature for selected calcined Co/ITQ-2 catalysts in a Cary 5 apparatus equipped with a "Praying Mantis" attachment from Harrick. $BaSO_4$ was used as reflectance standard.

The reduction behaviour of the supported cobalt phases was studied by hydrogen temperature-programmed reduction (H_2-TPR) in a Micromeritics Autochem 2910 apparatus. About 30 mg of sample was initially flushed with an Ar flow at room temperature for 30 min, then the gas was switched to 10 vol% H_2 in Ar and the temperature increased up to 1173 K at a heating rate of 10 K/min. A downstream 2-propanol/$N_{2(liq)}$ trap was used to retain the water generated during the reduction. The H_2 consumption rate was monitored in a thermal conductivity detector (TCD) previously calibrated using the reduction of CuO as reference. In the same equipment, the degree of reduction (DR) attained after reduction in flowing H_2 at 723 K for 10 h (the same pre-treatment applied prior to catalysis) has been estimated for selected catalysts following the experimental procedure detailed in [12].

Cobalt dispersion was determined by H_2-chemisorption at 373 K in an ASAP 2010C Micromeritics equipment by extrapolating the total gas uptakes in the H_2 adsorption isotherms at zero pressure, according to the procedure recommended by Bartholomew et al. [37]. Prior to adsorption, the samples (0.2–0.8 g) were pretreated in flowing He at 393 K for 1 h. Afterwards, the samples were reduced *in situ* by flowing pure H_2 and raising the temperature to 723 K at a heating rate of 1 K/min and maintaining this temperature for 10 h. After reduction, the samples were degassed at 1.3 Pa and the temperature lowered to 373 K. Co^0 particle sizes

($d(Co^0)_H$, where the suffix H stands for H_2-chemisorption), were estimated from the total amount of chemisorbed H_2, assuming a H/Co = 1 atomic ratio stoichiometry, Co content (from ICP-OES), complete reduction of cobalt (as ascertained by H_2-TPR) and a hemispherical particle geometry with a surface atomic density of 14.6 atoms/nm^2.

Medium resolution transmission electron microscopy (TEM) characterisation was performed with a *Philips CM10* device operated at 100 kV. High resolution (HR)TEM observation of selected samples was carried out in a *Tecnai G^2 field emission gun* equipment working at 200 kV. Before microscopy observation, the samples were prepared by suspending the solid in ethanol and submitting the suspension to ultrasonication for one minute. Afterwards, the suspension was let to slowly decant for two minutes and a drop was extracted from the top side and placed on a holey carbon-coated copper grid (200 mesh). The catalysts were previously reduced in flowing pure H_2 for 10 h at 723 K and stored at room temperature under a <1 vol% O_2/N_2 passivating atmosphere until sample preparation for microscopy. In the case of "spent" catalysts, the samples were extracted from the reactor after controlled stepwise exposure to air and directly transferred into a Schlenk flask under a passivating atmosphere. Metal particle size distributions were generated upon measurement of 150–200 particles coming from several images taken at different positions on the TEM grid. The surface-averaged mean particle size was calculated as $d(Co^0)_T = \frac{\sum_i n_i \cdot (d_i)^3}{\sum n_i \cdot (d_i)^2}$ (the suffix *T* stands for TEM) and the standard deviation as $\sigma = \sqrt{\frac{\sum_i n_i \cdot \left(d_i - d(Co^0)_T\right)^2}{\sum n_i}}$, where n_i is the frequency of occurrence of each d_i size.

The nature of surface metallic sites in selected model catalysts has been studied by infrared spectroscopy employing adsorbed CO as a probe molecule on a Bio-Rad FTS-40A spectrometer using a quartz infrared cell fitted with KRS-5 windows and an external furnace. Two kinds of experiments were performed prior to which the samples were submitted to a common pretreatment as follows: The catalysts were *ex situ* reduced in flowing pure H_2 at 723 K for 10 h and stored at room temperature under the passivating atmosphere. The solids were then pressed into self-supported wafers (5–10 mg/cm^2) and reduced again in the IR cell in flowing H_2 at 623 K for 2 h to avoid the presence of any oxidised Co species produced by passivation or reoxidation during sample handling. After the reductive pretreatment, the samples were outgassed under vacuum (ca. 10^{-5} mbar) at 673 K (50 K above the reduction temperature) to allow for the displacement of any H_2 adsorbed on the metal surface. The samples were then cooled to room temperature (RT) under vacuum. A set of experiments was performed at RT on the *in situ* reduced samples by stepwise pulsing different amounts (5–250 mbar) of CO (99.97% Purity, Linde) and recording the spectra after each dosage. After the last pulse (250 mbar CO), the samples were outgassed (10^{-5} mbar) at RT and the stepwise CO dosage repeated again from 5 to 250 mbar while recording the spectra. A second set of experiments was performed by flowing synthesis gas through the IR cell to study the catalysts *at work* in the FTS at atmospheric pressure. The reduced samples were exposed to a flow (50 mL/min) of $CO/H_2/Ar$ in a volume ratio 30/60/10 (Ar as inert diluent) at RT for 1 h to ensure a homogeneous atmosphere in the cell. Then, the temperature was increased stepwise to 383 K, 433 K, 473 K and finally to 493 K, that is, the temperature applied for the FTS in the high-pressure catalytic tests and maintained at this temperature for 4 h. The IR spectra were recorded after 5 min at each temperature and after 3, 120, 210 and 240 min on-stream at the final temperature (493 K). After the reaction, the catalysts were cooled to RT and outgassed before recording an evacuation spectrum.

2.2.1. Fischer–Tropsch synthesis catalytic tests

The Fischer–Tropsch synthesis (FTS) was carried out in a down-flow fixed-bed stainless steel reactor, as detailed elsewhere [10,12], employing 0.5–1.5 g of catalyst in the calcined form (0.25–0.42 mm pellet size) previously diluted with SiC granules (0.6–0.8 mm) to attain a bed volume of 6.4 cm^3. Prior to catalysis the catalyst was reduced *in situ* at atmospheric pressure in flowing pure H_2 (200 cm^3/(min g_{cat})) at 723 K for 10 h (1 K/min heating rate). After reduction the temperature was lowered to 373 K under the flow of H_2, and subsequently a flow of a mixture of CO, H_2 and Ar ($CO:H_2$:Ar volume ratio of 3:6:1, Ar used as internal standard) was established through the reactor, the reaction pressure increased up to 2.0 MPa, and the temperature raised up to 493 K at a rate of 4 K/min. A *pseudo*-steady catalytic behaviour was usually attained at time-on-stream (TOS) above 7–8 h. The space velocity was adjusted in each case to attain a *pseudo*-steady CO conversion of 10 ± 2%. C_1–C_{15} hydrocarbons, unreacted CO, Ar and CO_2 were analysed *on line* in a GC (Varian 3800) while heavier hydrocarbons were collected in a hot trap and analysed *off line* in the same GC as previously described [10,12]. Product yields and selectivities are given on a carbon basis.

3. Results and discussion

3.1. Characterisation of catalytic supports

Table 2 collects the textural properties of the pristine pure silica ITQ-2 support as well as the surface silylated S/ITQ-2 counterpart as determined by N_2 adsorption. ITQ-2 displays a rather high surface area (761 m^2/g) and pore volume (0.92 cm^3/g) while it displays a very low micropore volume (0.02 cm^3/g) consistent with the delayered nature of this material [32]. Thus, most of the measured B.E.T. surface area corresponds to external surface. The surface area and pore volume are decreased to a certain extent (28% and 20%, respectively) upon surface silylation as shown in Table 2 for S/ITQ-2, which obviously does not display remarkable microporosity. Table 2 also gathers the carbon content for both samples. As observed, the pristine calcined ITQ-2 sample contains 0.54 wt% C indicating that removal of the organic moieties coming from the swelling agents and the organic structure-directing agent employed in the synthesis of the MWW layered precursor is not completely accomplished after the air-calcination at 823 K. The surface silylation leads to an increase in the carbon content up to 7.0 wt% which is consistent with a surface coverage of ca. 1.5 anchored trimethylsilyl organic groups per nm^2. TEM characterisation confirms the delayered nature of the silylated support. Fig. 1 depicts a representative TEM image for S/ITQ-2 showing the presence of individual plate-like nanosheets with limited contrast owing to their very fine thickness as a result of the delamination of the layered MWW precursor, which typically displays a platelet aspect. Additionally, some fibre-like morphologies are also found probably derived from original crystals displaying aspect ratios closer to a needle-like morphology.

Table 2
Textural properties and carbon content for the pristine and silylated ITQ-2 support.

Sample	Area (B.E.T.) (m^2/g)	PV[a] (cm^3/g)	MPV[b] (cm^3/g)	Carbon content (wt%)
ITQ-2	761	0.92	0.02	0.54
S/ITQ-2	546	0.74	0.02	7.00
SiO_2	387	0.80	n.d.[c]	n.d.

[a] Total pore volume.
[b] Micropore volume.
[c] Not determined.

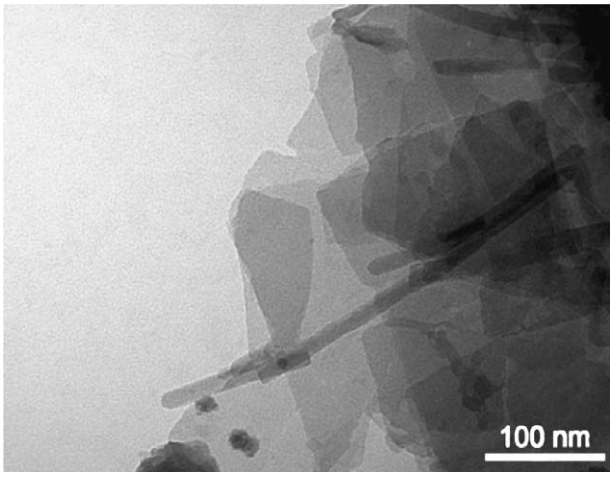

Fig. 1. Representative TEM image for the surface-silylated ITQ-2 support (S/ITQ-2) showing the presence of zeolitic nanosheets obtained by delamination of the layered MWW precursor.

On the other hand, the employed amorphous commercial silica gel displays a B.E.T. surface area of 387 m^2/g and a pore volume of 0.8 cm^3/g as also gathered in Table 2.

3.2. Metal content and dispersion in Co catalysts

Cobalt contents, experimentally determined by ICP-OES, agree well (within ±10% error) with the nominal metal loadings for all catalysts, as collected in Table 3. This indicates that cobalt is nearly quantitatively deposited on the S/ITQ-2 support from the reverse micellar medium employed to *ex*-support disperse the metal. Results in Table 3 also show that calcined Co/ITQ-2 model catalysts display carbon contents in the 0.52–0.83 wt% range essentially due to the residual carbonaceous species already found in the pristine ITQ-2 support after its calcination (Table 2), as previously mentioned. Nevertheless, a small increase in carbon content of up to 0.29 wt% is found in some samples indicating that a complete removal of the organic moieties (i.e. anchored trimethylsilyl groups or remaining surfactant from the reverse microemulsion) was not always accomplished upon air-calcination at 773 K. This increase in carbon content seems to take place randomly and no correlation between the carbon gain and the amount of surfactant employed in the catalyst preparation (Table 1) is found. Finally, 30%Co/SiO_2 is C-free as no organic substances were employed in its preparation.

As already mentioned in Section 2, the characteristics of the reverse micellar medium employed in the preparation of the Co/ITQ-2 model catalysts were intentionally varied aiming at obtaining a battery of catalysts with different metal dispersions in the range where particle size effects have been claimed to become apparent for the FTS (i.e. <10 nm). As seen in Table 1, the surfactant concentration in the organic phase ($[Surf]_{org}$) is progressively increased while the water-to-surfactant molar ratio (R) and the molar concentration of metal precursor in the aqueous core of the reverse micelles ($[Co]_{aq}$) are decreased to gradually increase metal dispersion in the order 10%Co/ITQ(1) < ··· < 10%Co/ITQ(5), as will be shown later. In order to further increase metal dispersion (i.e. decrease Co particle size), the stoichiometric excess of hydrazine has been complementarily increased from 8 to 10 and 16-folds to obtain samples 10%Co/ITQ(6) and 10%Co/ITQ(7), respectively. The higher concentration in hydrazine enhances the rate of nucleation processes against the corresponding rate of cluster growth [38]. This effect, along with the enhanced "cobalt compartmenting" exerted by the metal and surfactant concentrations in the aqueous and organic phases, respectively, should allow for a further increase in metal dispersion.

Metal dispersion in oxidised Co catalysts was studied by means of XRD. The spinel Co_3O_4 (JCPDS 42-1467) was the only crystalline Co phase detected for samples 30%Co/SiO_2 and 10%Co/ITQ(1–5). Besides, as shown in Fig. 2 as a detailed diffractogram showing the most intense (3 1 1) peak of Co_3O_4 in selected catalysts, differences in line broadening are evident, as a result of changes in metal particle size. An analysis performed on the diffractograms by applying the Scherrer's equation shows a cobalt oxide particle size, $d(Co_3O_4)_X$, of 125 nm for 30%Co/SiO_2. This relatively low metal dispersion is in concordance with the employment of a commercial nanosized Co_3O_4 powder in the preparation of this model catalyst. Additionally, $d(Co_3O_4)_X$ progressively decreases from 12.5 to 5.9 nm, corresponding to $d(Co^0)_X$ = 9.4–4.4 nm in the reduced catalysts (Table 4) for samples 10%Co/ITQ(1–5), as a result of the particle size control exerted by the reverse microemulsions employed in their preparation. By contrast, no XRD-detectable Co oxide phases were evident in samples 10%Co/ITQ(6) and 10%Co/ITQ(7) which might be related to the absence of Co_3O_4 or to its presence as XRD-silent very small crystallites, in line with the higher metal dispersion expected for these catalysts according to their preparation parameters (Table 1). Very weak diffractions at 2θ = 36.6° and 44.5°, which might be ascribed to α-Co_2SiO_4 (JCPDS 15-0865), are found for 10%Co/ITQ(7) (see Fig. S1 in the Supplementary material).

Metal dispersion was also determined on pre-reduced catalysts by H_2-chemisorption from the total H_2-uptakes. The corresponding

Table 3
Cobalt loadings and carbon contents as determined by ICP-OES and elemental analysis, respectively.

Catalyst	Co (wt%)	Carbon content (wt%)
10%Co/ITQ(1)	9.3	0.64
10%Co/ITQ(2)	9.0	0.52
10%Co/ITQ(3)	9.6	0.74
10%Co/ITQ(4)	10.1	0.83
10%Co/ITQ(5)	10.5	0.54
10%Co/ITQ(6)	9.4	0.61
10%Co/ITQ(7)	9.6	0.58
30%Co/SiO_2	28.7	n.d.[a]

[a] Not determined.

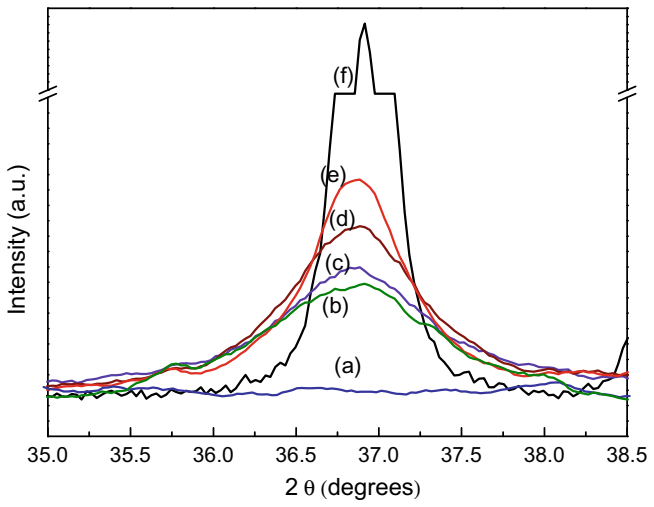

Fig. 2. X-ray diffractograms for (a) S/ITQ-2 (support) and the calcined catalysts (b) 10%Co/ITQ(5), (c) 10%Co/ITQ(4), (d) 10%Co/ITQ(2), (e) 10%Co/ITQ(1) and (f) 30%Co/SiO_2, showing the differences in line broadening for the (3 1 1) diffraction of Co_3O_4.

Table 4
Results for metal dispersion in the model catalysts as derived from XRD, TEM and H_2-chemisorption characterisation.

Catalyst	XRD		H_2-Chemisorption			TEM	
	$d(Co_3O_4)$ (nm)	$d(Co^0)_X$[a] (nm)	H_2-uptake (μmol/g)	D[b] (%)	$d(Co^0)_H$ (nm)	$d(Co)_T$[c] (nm)	σ[d] (nm)
30%Co/SiO_2	125	94	16.6	0.7	141	183	56
10%Co/ITQ(1)	12.5	9.4	83	9.6	10.4	12.8	3.4
10%Co/ITQ(2)	9.9	7.4	82	11.2	8.9	8.2	2.0
10%Co/ITQ(3)	9.1	6.8	122	13.6	7.3	n.d.	n.d.
10%Co/ITQ(4)	6.8	5.1	161	17.8	5.6	6.3	1.5
10%Co/ITQ(5)	5.9	4.4	n.d.[e]	n.d.	n.d.	n.d.	n.d.

[a] Mean Co^0 particle size as estimated from the corresponding $d(Co_3O_4)$ by applying the molar volume correction: $d(Co^0) = 3/4\ d(Co_3O_4)$.
[b] Metal dispersion.
[c] Surface-averaged mean particle size, corrected by the observed surface or total reoxidation.
[d] Standard deviation for the particle size distribution.
[e] n.d. = Not determined.

metal dispersions (D) and mean Co particle sizes ($d(Co^0)_H$) are collected in Table 4. As observed, 30%Co/SiO_2 displays low metal dispersion (0.7%) corresponding to large $d(Co^0)_H = 141$ nm in line with the XRD results. Nevertheless, $d(Co^0)_H$ is substantially higher than that estimated from the XRD characterisation on the corresponding calcined counterpart ($d(Co^0)_X = 94$ nm), which suggests that metal sintering took place upon H_2 reduction of this sample, owing to a limited interaction between the Co_3O_4 powder and the spherical SiO_2 particles. On the other hand, 10%Co/ITQ(1–4) model catalysts display metal dispersions in the range 9.6–17.8%, corresponding to $d(Co^0)_H$ ranging 10.4–5.6 nm. In this case, $d(Co^0)_H$ estimated by chemisorption nicely agrees with the values derived from the XRD analysis on the calcined samples, though $d(Co^0)_H$ are systematically slightly higher (7–20%) than the corresponding $d(Co^0)_X$, pointing to the occurrence of a certain but limited sintering of Co nanoparticles during reduction.

Additionally, TEM was performed on pre-reduced and passivated catalysts. Fig. 3 shows representative medium-resolution TEM micrographs for 10%Co/ITQ(4), 10%Co/ITQ(2), 10%Co/ITQ(1) and 30%Co/SiO_2 model catalysts. As shown in the pictures, round-shaped cobalt nanoparticles (higher contrast) dispersed on the ITQ-2 nanosheets (less contrasted against the carbon coating of the TEM grid) are observed in all the Co/ITQ-2 catalysts. The particle size distributions, also depicted in Fig. 3, show a nearly monomodal, rather narrow Gaussian-like behaviour with $d(Co^0)_T$ of 12.8, 8.2 and 6.3 nm for 10%Co/ITQ(1), 10%Co/ITQ(2) and 10%Co/ITQ(4), respectively. As collected in Table 4, the standard deviations for the surface-averaged particle size distributions lay in the range 1.5–3.4 nm (corresponding to 22–24% in all cases) for the Co/ITQ-2 catalysts and it increases with increasing Co particle size, maybe, as a result of a decreased homogeneity in the metal particle size when larger micelles (higher *R*, see Table 1) are employed in the microemulsion. The values for $d(Co^0)_T$ have been estimated by correcting for the volume contraction of a 3-nm thick CoO surface layer observed for passivated 10%Co/ITQ(1) and 10%Co/ITQ(2), while total reoxidation to CoO has been considered for correcting the particle size measured in 10%Co/ITQ(4), for which the smaller particle size makes it more prone to undergo reoxidation during passivation and sample handling. Indeed, Fig. 4 depicts a representative HRTEM image for 10%Co/ITQ(4) showing metal nanocrystals of 6–8 nm in size displaying a lattice spacing of 2.1 Å, typical of the (200) crystallographic plane of CoO, thus, corresponding to Co^0 nanoparticles of size 4.5–6 nm, which have been completely reoxidised. The relatively lower TEM contrast found for the Co nanoparticles in 10%Co/ITQ(4) (Fig. 3a) can also be a consequence of their complete reoxidation. No correction for the passivation layer has been considered for the less dispersed 30%Co/SiO_2 catalyst displaying a $d(Co^0)_T$ of 183 nm, which is in better agreement with the value obtained from H_2-chemisorption ($d(Co^0)_H = 141$ nm) than with that derived from XRD ($d(Co^0)_X = 94$ nm), thus confirming that significant metal sintering has occurred during its reduction. The particle size distribution in 30%Co/SiO_2 is also significantly broader than in the case of the model Co/ITQ-2 catalysts prepared from reverse microemulsions. As shown in Fig. 3d, large metal crystals are found exclusively on the outer surface of the porous silica particles, as expected from the procedure employed to prepare this sample.

3.3. Particle size-dependent nature and reducibility of oxidised Co species

The reduction behaviour of the model Co/ITQ-2 and Co/SiO_2 catalysts has been studied by means of H_2-TPR. Fig. 5a shows the H_2-TPR profiles for catalysts vertically arranged according to their $d(Co_3O_4)_X$. Samples 10% Co/ITQ(6-7) which do not display XRD-detectable Co_3O_4 species are also included in the picture and have been placed considering the expected trend in metal dispersion based on the parameters of the reverse microemulsion employed in their preparation (Table 1). As observed, two main H_2-consumptions take place in the temperature range 500–720 K for the model catalysts 30%Co/SiO_2 and 10%Co/ITQ(1–5) which are known to correspond to the two-step reduction of Co_3O_4: $Co_3O_4 \rightarrow CoO$ (peak I at temperatures 530–595 K) and $CoO \rightarrow Co^0$ (peak II at temperatures 579–714 K). This assignment is also supported by the H_2 consumption ratio (peak II)/(peak I) that lays in the range 3–3.7 for all the samples, roughly according to the expected stoichiometric ratio of 3. As observed in Fig. 5a, there is a continuous shift towards higher temperatures for both peaks I and II with decreasing $d(Co_3O_4)_X$. Fig. 5b depicts the peaking-temperatures from TPR profiles against $d(Co_3O_4)_X$ for all the Co/ITQ-2 catalysts. The point corresponding to peak II for catalyst 10%Co/ITQ(1) has not been included (dashed line) due to the fact that this sample displays two maxima in the H_2-TPR profile in the temperature range where the other samples exhibit a single reduction feature (peak II). As observed, the temperatures for the two reduction steps of Co_3O_4 to Co^0 (peaks I and II) increase with decreasing $d(Co_3O_4)_X$ in the range 12.5–5.9 nm. No significant reduction features in the higher temperature regime (>800 K) are found for catalysts displaying $d(Co_3O_4)_X$ from 125 to 6.8 nm. In contrast, when the Co_3O_4 particle size is further decreased to 5.9 nm in 10%Co/ITQ(5), an additional intense peak develops at 840 K (peak III) while a weak H_2 consumption occurs at very high temperature of 1020 K (peak IV). Further increasing metal dispersion (i.e. decreasing Co particle size) in 10%Co/ITQ(6) nearly depletes the reduction features for Co_3O_4 below 800 K, in agreement with the absence of X-ray diffractions for Co_3O_4, and peak III develops at 884 K, with an additional less intense shoulder at 1011 K (peak IV). Finally, forcing the preparation towards still higher metal dispersion in 10%Co/ITQ(7) appears to shift the so-called peak III towards a higher temperature (905 K) and sharply reduces its relative intensity against the predominant

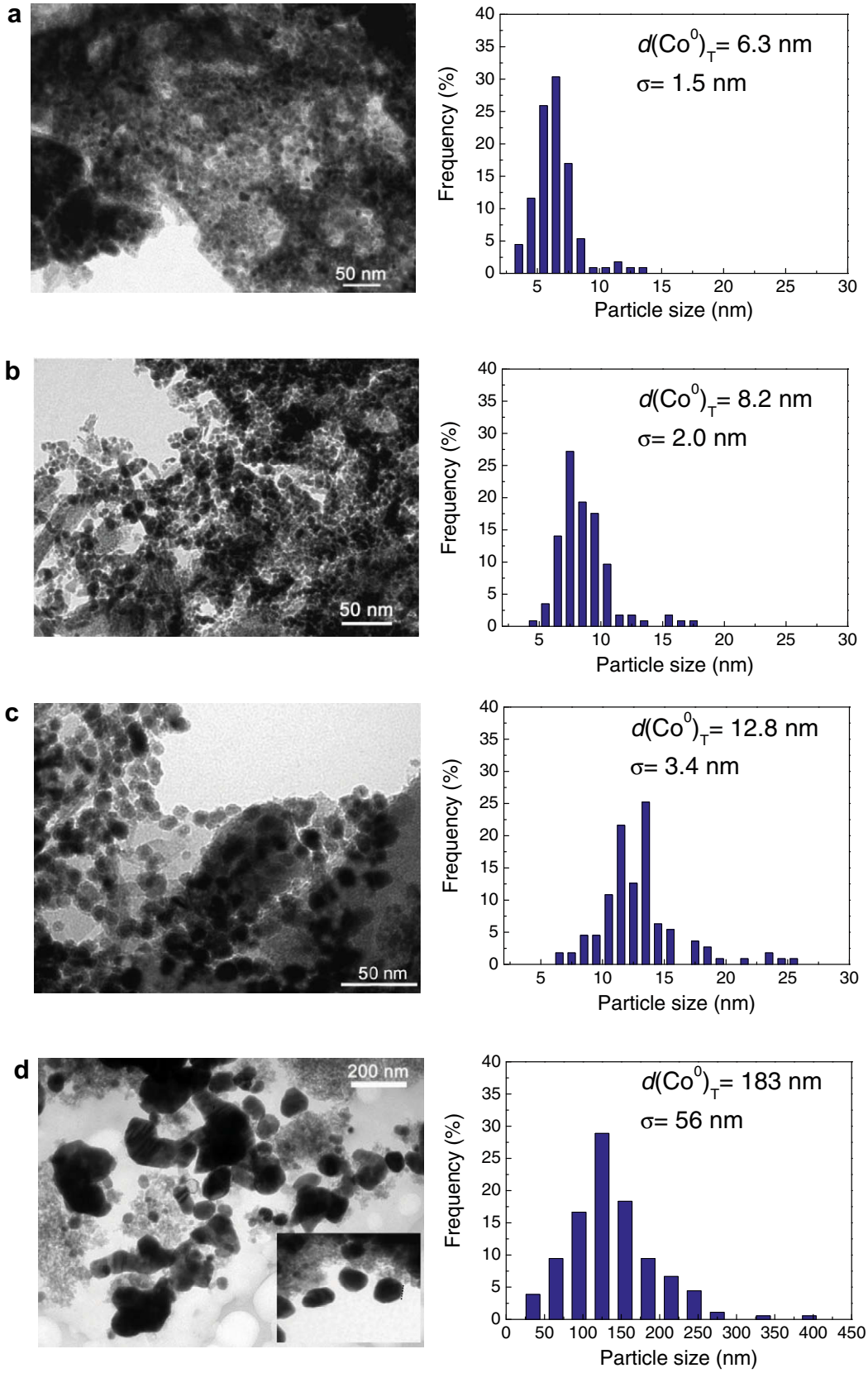

Fig. 3. Representative TEM images and the corresponding particle size histograms for pre-reduced and passivated (a) 10%Co/ITQ(4), (b) 10%Co/ITQ(2), (c) 10%Co/ITQ(1) and (d) 30%Co/SiO_2 catalysts.

high temperature (>950 K) peak IV which, in this case, appears as an intense band peaking at 980 K with a shoulder at 1036 K.

It can be perceived in Fig. 5b that 10%Co/ITQ(5), displaying a $d(Co_3O_4)_X$ of 5.9 nm, is a transition sample between the less

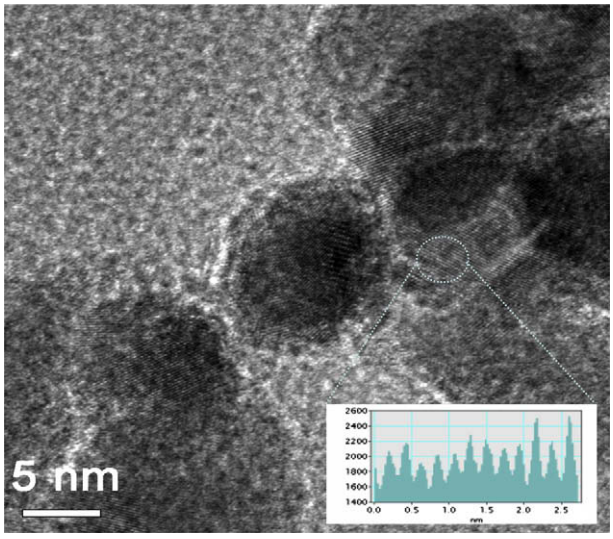

Fig. 4. HRTEM image for the pre-reduced and passivated 10%Co/ITQ(4) catalyst as well as the lattice-spacing profile evidencing re-oxidation to CoO.

dispersed catalysts displaying exclusively the reduction peaks for Co_3O_4 (peaks I and II) and the samples exhibiting higher metal dispersion, which display merely reduction features above 800 K (peaks III and IV). As already commented for peaks I and II, it can be noticed that the so-called peak III shows a dispersion-dependent peaking-temperature (Fig. 5b). By contrast, the higher temperature features (peak IV at 980–1036 K) show no evident dispersion dependence.

It is clearly derived from the H_2-TPR profiles that a coherent evolution in the size and nature of cobalt species takes place with the metal dispersion for the battery of Co/ITQ-2 model catalysts, likely due to the fine control in metal dispersion attained by the employed synthetic methodology. Besides, this trend allows to "isolate" some predominant reduction features in certain samples that are expected to correspond to nearly single cobalt species. DR UV–vis spectroscopy has been used to elucidate this dispersion-dependent nature of cobalt species in the calcined monodispersed Co/ITQ-2 catalysts. This information is especially desirable for the Co species that reduce above the temperatures typically applied in the reductive pre-treatments prior to catalysis (573–773 K) and which are known to be catalytically inactive for FTS [14,15]. Fig. 6 collects the UV–vis spectra for selected calcined Co/ITQ-2 catalysts. As depicted there, the spectra show several broad features in the 300–800 nm range due to ligand-to-metal charge transfer events and d–d electronic transitions associated with Co ions. Catalysts 10%Co/ITQ(1 and 4) show broad bands at 430 and 730 nm (with a shoulder at 670 nm), which are ascribed to oxygen-to-metal charge transfers for Co^{2+} and Co^{3+} ions, respectively, in the lattice of the spinel Co_3O_4 [39]. No additional bands in the region 450–650 nm are evident, in agreement with Co_3O_4 as the only cobalt phase in these samples, as discussed on the basis of XRD and H_2-TPR results. On the other extreme, the most dispersed sample 10%Co/ITQ(7) shows a triplet peaking at 522, 579 and 631 nm that are typical, respectively, for the $^4A_2 \rightarrow {}^2T_1$, $^4T_1$ and $^2T_2$ electronic d–d transitions in Co^{2+} ions having pure tetrahedral coordination in Co_2SiO_4 silicates [40]. Thus, in this sample, cobalt has been completely incorporated in the bulk of the ITQ-2 support as single Co^{2+} ions during calcination. According to this, peak IV in the H_2-TPR profiles can be assigned to "bulk" Co_2SiO_4 silicates and the fact that cobalt no longer exists as surface clusters agrees with the absence of a dispersion-dependence for reduction temperature of peak IV (Fig. 5b). Distinctly, 10%Co/ITQ(6) displays almost no band at 631 nm while the more energetic band is slightly down-shifted to 496 nm. This type of distortion might be related to the coexistence of Co^{2+} ions both in tetrahedral and in octahedral coordinations or, more likely, to a partial distortion of the tetrahedral coordination in a Co silicate due to some extra ligands for Co^{2+}, such as OH groups from the silanols existing at

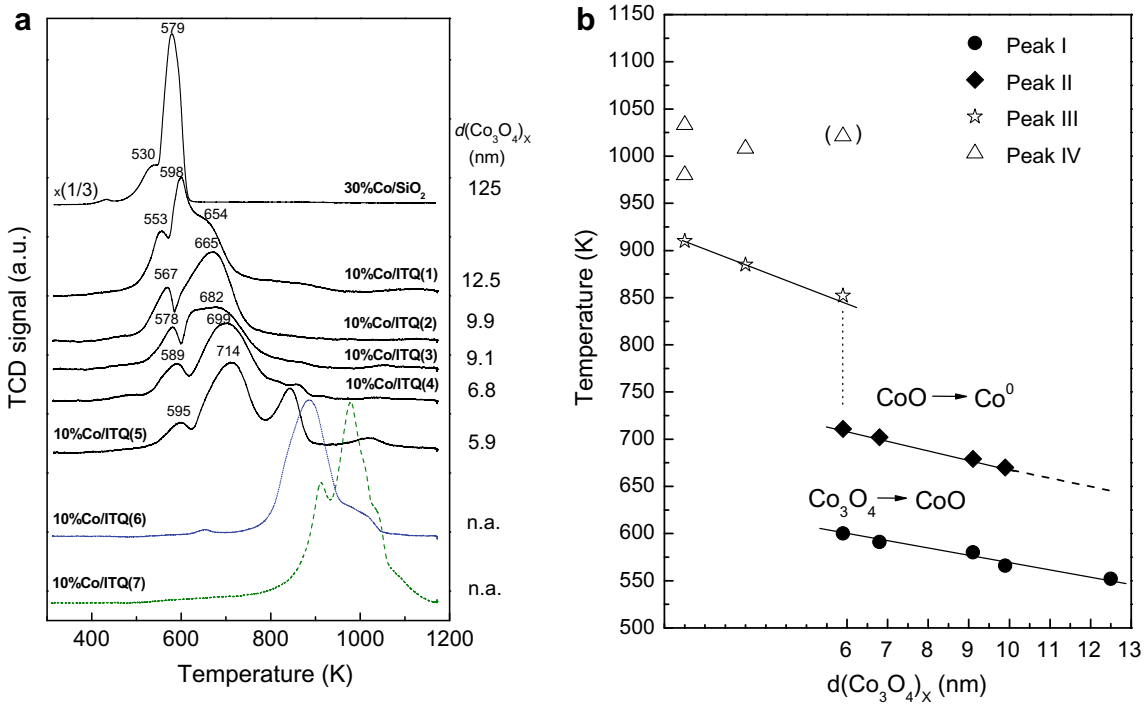

Fig. 5. (a) H_2-TPR profiles for the Co/ITQ-2 and Co/SiO_2 model catalysts; and (b) evolution of the temperature for the reductive features identified by H_2-TPR with metal particle size for the model Co/ITQ-2 catalysts. (n.a.: not available owing to the absence of XR diffractions for Co_3O_4).

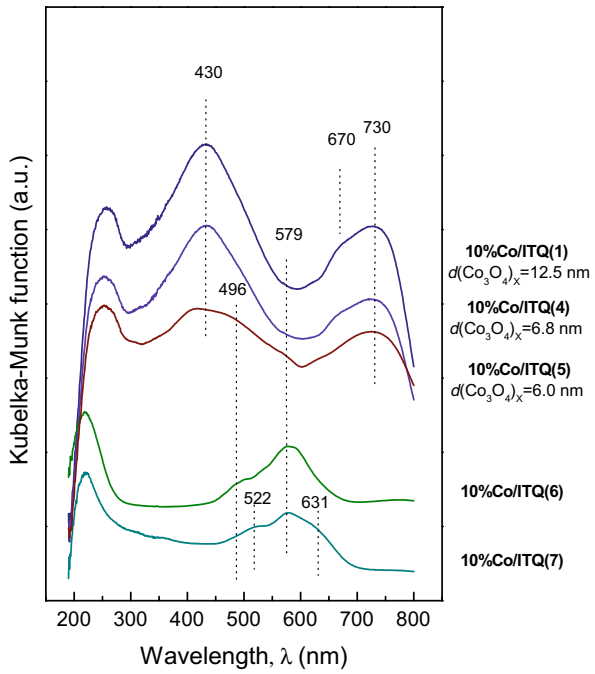

Fig. 6. DR UV–vis spectra for selected samples, displaying distinct metal dispersion, in their calcined form.

the surface of the siliceous support [39,41]. Thus, it appears that the Co silicate species existing in 10%Co/ITQ(6) are present as small clusters on the surface of the ITQ-2 support, unlike the bulk Co_2SiO_4 existing in 10%Co/ITQ(7). This assumption concurs also with the dispersion-dependence observed in Fig. 5b for the TPR peak III, which is predominant in this catalyst. The absence of bands due to Co_3O_4 in this sample discards the assignment of this peak III reduction at 850–910 K to Co_3O_4 or CoO species very small in size, highly interacting with the silica support, as proposed in previous works [42]. Finally, 10%Co/ITQ(5), as a transition sample, displays the bands related to the Co_3O_4 spinel, along with shoulders at 496 and 579 nm associated to the presence of the mentioned surface *hydroxy*-silicates, existing probably at the contact boundary between the Co_3O_4 nanoparticles and the ITQ-2 support.

The degrees of reduction (DR) of selected samples, as estimated by H_2-TPR after *in situ* submitting the catalysts to the same reductive pre-treatment applied prior to catalysis (723 K, 10 h), increased from 87% to 96% when increasing $d(Co_3O_4)$ from 6.8 to 12.5 nm for catalysts 10%Co/ITQ(4) to 10%Co/ITQ(1), while it is 100% for the low-dispersed 30%Co/SiO_2 sample. These high values of DR ensure no significant contribution from unreduced (ionic) Co species during catalysis for these model catalysts.

As a summary, the homogeneous metal dispersion attained in the Co/ITQ-2 model catalysts, together with the H_2-TPR and DR UV–vis results, has allowed to progressively study how the nature and the reducibility of the supported Co species evolve with particle size up to high dispersion levels. It is concluded that the combination of the *ex*-support micellar synthesis and the surface silylation of the ITQ-2 support leads to highly reducible catalysts in the range of Co_3O_4 particle size of 6.8 to 12.5 nm. Moreover, this model system has permitted to unambiguously conclude that the activation energy for the reduction steps of this cobalt spinel is particle size dependent. This conclusion, although it may seem obvious at the view of previous literature reporting that smaller Co_3O_4 particles are less reducible than larger ones [9,14], is in the present case not disturbed by high temperature reduction features ascribed to mixed Co–Si compounds that typically coexist with Co oxides in highly dispersed catalysts prepared by conventional methods, due to the inherent broad size distributions. The enhanced reducibility thanks to the protective organic capping of the ITQ-2 silanols during Co_3O_4 crystallisation finds its limit at $d(Co_3O_4)$ around 5.9 nm, as for sample 10%Co/ITQ(5). For Co_3O_4 particles below this limit, the interaction between the supported Co phases and the ITQ-2 support promotes their partial reaction during the final calcination steps, when the protective capping organic groups have been burnt off, leading firstly to surface *hydroxy*-silicates, probably at the boundary of Co_3O_4 and the siliceous carrier, and to bulk Co_2SiO_4 when metal dispersion is further increased, as in 10%Co/ITQ(7).

3.4. Catalytic activity in the Fischer–Tropsch synthesis

The series of highly reducible monodispersed Co/ITQ-2 model catalysts and the low dispersed 30%Co/SiO_2 sample are excellent candidates to study particle size effects in FTS. Their catalytic activity in the FTS at $P = 2.0$ MPa, $T = 493$ K has been examined. Only highly reducible catalysts, displaying DR values in the range 87–100%, were tested to ensure that the catalytic results are not disturbed by the presence of any significant amount of oxidised Co species that are known to display decreased activity and enhanced selectivity towards methanation [7,9,15]. In all the experiments, the space velocity (GHSV) was adjusted to set the steady CO conversion to a relatively low value of ca. 10%. This rather low conversion level has been chosen to limit the changes in the gas composition through the catalytic bed and to avoid the existence of a high water partial pressure as water, the main sub-product of the FTS, has been reported to *auto-catalytically* enhance the reaction rate in the Co/SiO_2-catalysed Fischer–Tropsch synthesis when present in appreciable amounts at high CO conversion levels [43]. Limiting the P_{H_2O} is also desirable from the standpoint of avoiding re-oxidation of the smallest cobalt nanoparticles during the reaction, although Co re-oxidation during FTS has been discarded in catalysts displaying Co particle sizes as small as 6 nm under industrially relevant FTS conditions [44].

Table 5 collects the catalytic results for selected model catalysts. As shown there, the less dispersed sample 30%Co/SiO_2 ($d(Co^0)_H = 141$ nm) displays a cobalt-time-yield (CTY) of 3.3×10^{-3} mol CO/(g_{Co} h), much lower than the CTY of Co/ITQ-2 catalysts (14×10^{-3}–53×10^{-3} mol CO/(g_{Co} h)), as it may be expected from the much lower metal dispersion of the former. Nevertheless, the expected increase in CTY when decreasing $d(Co^0)$ no longer applies for the series of Co/ITQ-2 model catalysts. Indeed, CTY continuously decreases from 10%Co/ITQ(1)–10%Co/ITQ(4), that is, with decreasing metal particle size from $d(Co^0)_H = 10.4$ nm to $d(Co^0)_H = 5.6$ nm, and thus when the number of exposed metallic Co^0 sites is doubled (see H_2 uptakes in Table 4). This decay in the CTY is thus related to a decrease in the intrinsic site-activity with decreasing $d(Co^0)$. Fig. 7 depicts the variation of the *turnover frequency* (TOF), based on H_2-chemisorption, versus $d(Co^0)_H$. TOF

Table 5
Steady FTS activity and selectivity for selected model catalysts in the Fischer–Tropsch synthesis. Reaction conditions: $T = 493$ K, $P = 2.0$ MPa., GHSV adjusted to obtain a CO conversion level of (10 ± 2)%.

Catalyst	Cobalt-time yield (10^{-3} mol CO/g_{Co} h)	TOF[a] (10^{-3} s^{-1})	Selectivity (%C)		
			CO_2	CH_4	C_{5+}
30%Co/SiO_2	3.3	8.2	1.0	8.7	78.9
10%Co/ITQ(1)	53	8.6	1.1	18.9	61.6
10%Co/ITQ(2)	48	6.8	0.8	16.6	63.0
10%Co/ITQ(3)	27	3.3	0.7	14.7	66.4
10%Co/ITQ(4)	14	1.2	0.6	14.0	68.8

[a] Estimated from H_2-chemisorption results.

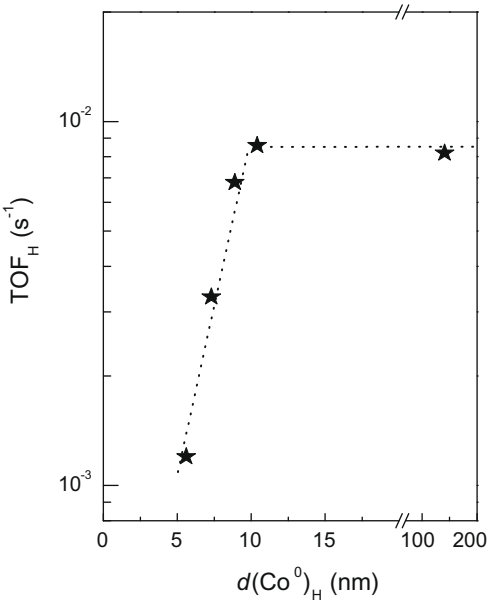

Fig. 7. Evolution of TOF based on H_2-chemisorption with Co^0 particle size. Reaction conditions: T = 493 K, P = 2.0 MPa, X_{CO} = 10%. Lines are guides to the viewer.

increases with increasing $d(Co^0)_H$ for sizes in the range 5.6–10.4 nm and then remains invariant up to $d(Co^0)$ = 141 nm.

Other works previously reported a decrease in TOF for cobalt particles below ca. 10 nm in size [16–18], although the presence of unreduced Co species in the highly dispersed catalysts used in these studies adds uncertainty in assigning the observed results to a true particle-size effect. Recently, Bezemer et al. [19] prepared model catalysts by supporting cobalt on carbon nanofibres (Co/CNFs) and attained high reducibilities for catalysts with mean Co particle sizes as small as 2–3 nm. Using this catalytic system, they found an increase in TOF with increasing $d(Co^0)$ in the range of 2.6 to 8–9 nm and then an invariant site-activity for larger particle sizes (9–20 nm) in the Fischer–Tropsch synthesis at 3.5 MPa and 483 K. This phenomenon has been referred to as "non-classical" particle size effect as it takes place at particle sizes well above those at which the *classical structure sensitivity* [23] occurs as a result of differences in the relative population of distinct metallic surface sites (surface crystalline anisotropy) or exposed crystal planes [45] and which manifests typically for metal particle sizes below 3–4 nm [46,47]. In contrast, the size-dependence for TOF persists up to particle sizes of 8–10 nm, according to our results and those previously reported by Bezemer et al. [19].

It should be stated that initial TOF values (extrapolated to TOS = 0) show exactly the same trend with $d(Co^0)$ as that shown in Fig. 7 for the pseudo-steady TOF, which discards any significant contribution from a particle size-dependent metal sintering rate during catalysis.

Finally, it is remarkable that the TOF values reported in Table 5 are 2–3 times lower than those typically reported in previous papers under similar reaction conditions [3,10,19]. According to an on-going research in our laboratory [48], these differences can be accounted for by considering the higher calcination temperature (773 K) required in the preparation of the present model catalysts, which finally leads (after reduction) to decreased TOF values as compared to catalysts calcined at lower temperatures (T < 623 K) or directly reduced in H_2 (not calcined). The difference in the conversion level at which the TOF values are calculated in each work can also have an extra (though lower) contribution to this gap in the TOF values, as it is known that the H_2O product auto-catalytically enhances reaction rates in Co/SiO_2 systems at higher conversion levels [43].

Regarding the product selectivity (at X_{CO} = 10%), the results collected in Table 5 show that the selectivity to methane decreases from 18.9% to 14.0% while the selectivity to the desired long-chain hydrocarbons (C_{5+}) increases from 61.6% to 68.8% for the tested Co/ITQ-2 catalysts in the order 10%Co/ITQ(1)–10%Co/ITQ(4), that is, when particle size is increased from 5.6 to 10.4 nm. Besides, unlike the trend observed for TOF, further increasing metal particle size up to 141 nm (30%Co/SiO_2) still leads to an important increase in the selectivity to the C_{5+} fraction (up to 78.9%) at expenses of the lighter hydrocarbons (S_{CH4} = 8.7%). The results obtained with our model Co-based catalysts concur with previous ones showing an increase in the selectivity to C_{5+}hydrocarbons with increasing Co^0 particle size in the range of constant TOF [19]. At this point, it should be mentioned that the differences in the volumetric density of Co^0 sites, coming from the different $d(Co^0)_H$ (and Co loading in the case of 30%Co/SiO_2), which might affect the probability for α-olefin readsorption [49], cannot be used to explain the differences in product selectivities. Indeed, the opposite trend should be expected in this case as the less dispersed catalysts (lower site density) should display a lower probability for α-olefin readsorption and thus a lower selectivity towards long-chain hydrocarbons. Thus, the differences in product selectivity observed in our model catalysts are likely an intrinsic characteristic related to Co^0 particle size. Finally, it should be mentioned that there are not significant changes in the selectivity to CO_2 for all catalysts (0.6–1.1%) and there is no correlation with $d(Co^0)$. Unreduced oxidic Co species have been claimed as responsible for an enhanced activity towards the *water gas shift reaction* (WGSR: $CO+H_2O \rightarrow CO_2 + H_2$), which produces CO_2 and also enhances methanation [36]. This enhanced CO_2 production does not take place in our catalytic experiments as an indirect proof of the high reducibility of the employed model catalysts.

Elucidating the origin for the non-classical structure sensitivity in the FTS still remains as a challenging scientific goal. Here, we have employed *in situ* and *at work* CO-FTIR spectroscopy to study the evolution of CO adsorption sites during catalysis, for samples displaying different particle sizes and TOFs, as an approach to understand the particle size-dependent site-activity.

3.5. In situ and at work CO-FTIR spectroscopy

3.5.1. Adsorption sites on as-reduced catalysts

FTIR of adsorbed CO (CO-FTIR) has been extensively used to study the nature of surface sites in most transition metal catalysts, since it is known that the spectral characteristics of the CO probe molecule strongly depend on the electronic state of the adsorption sites [50].

In the present work, selected model cobalt catalysts have been studied by CO-FTIR at RT to investigate the nature of their surface cobalt sites after submitting the samples to the same H_2-reduction pre-treatment applied prior to catalysis (see Section 2). Considering the site-activity trend shown in Fig. 7, three samples covering both the particle size range studied (5.6–141 nm) and the range for TOF values found in the catalytic experiments have been selected for the CO-FTIR study: 30%Co/SiO_2 ($d(Co^0)_H$ = 141 nm), 10%Co/ITQ(1) ($d(Co^0)_H$ = 10.4 nm), both displaying similar TOF, and 10%Co/ITQ(4) ($d(Co^0)_H$ = 5.6 nm) which shows the lowest TOF among the investigated samples. Due to opaqueness issues, the high metal loading 30%Co/SiO_2 sample was diluted with the required amount of SiO_2 to yield a 10 wt% Co loading. The resulting sample, which is exclusively used in the CO-FTIR studies, is hereafter denoted as 10%Co/SiO_2.

Room temperature FTIR spectra of CO adsorbed at low CO dosage (5 mbar) on the reduced samples are collected in Fig. 8. Two

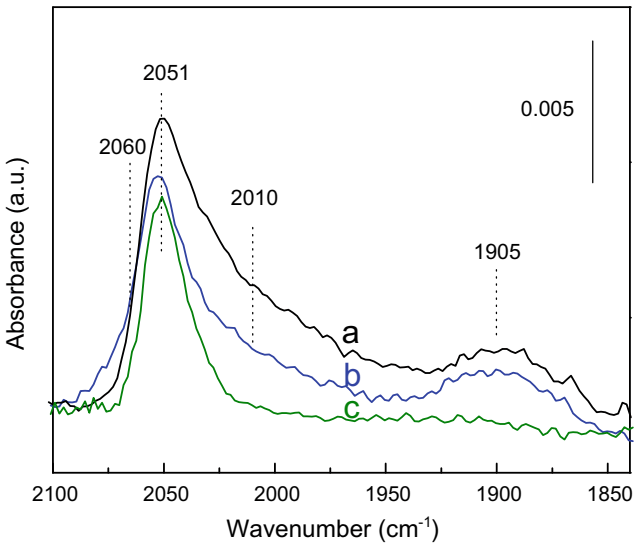

Fig. 8. Room temperature FTIR spectra of adsorbed CO on pre-reduced (a) 10%Co/ITQ(1), (b) 10%Co/ITQ(4) and (c) 10%Co/SiO_2 model catalysts at low CO dosage (P_{CO} = 5 mbar).

main adsorption peaks at ca. 2051 and 1905 cm^{-1} are observed for the catalysts, which are ascribed to CO adsorbed in linear and bridge forms, respectively, on metallic cobalt sites [51,52]. The band at ca. 2050 cm^{-1} has been previously assigned to CO linearly adsorbed on top of *fcc* Co^0 supported on SiO_2 [53], which agrees with the prevalence of this crystalline phase in our model catalysts, as ascertained by XRD on the reduced samples (not shown). The predominance of this band suggests its specific assignment to Co^0 planar sites on a highly exposed *fcc* facet such as (1 1 1). The band at 2051 cm^{-1} appears clearly asymmetric with a shoulder at a lower frequency (ca. 2010 cm^{-1}) in 10%Co/ITQ(1) and 10%Co/ITQ(4) catalysts, which is hardly observed in the low-dispersed 10%Co/SiO_2 sample. Low frequency IR bands of CO linearly adsorbed on Co^0 surfaces have been assigned in the literature to low-coordinated surface sites located on more open low-index surface crystallographic planes or steps and corners, having an enhanced electron back-donation from the d metallic orbitals to the π^* antibonding molecular orbital of CO [50,54,55]. The presence of a much higher density of such coordinatively unsaturated Co^0 sites in the two Co/ITQ-2 catalysts agrees with the significantly smaller particles existing on these micelle-synthesised samples in contrast to the much larger particles, exposing preferentially well-defined crystal facets, in the 10%Co/SiO_2 sample. From the relative band intensities, no significant difference in the proportion of defect sites is evidenced in Fig. 8 for 10%Co/ITQ(4) and 10%Co/ITQ(1). This, which might seem surprising considering their difference in $d(Co^0)$ (Table 4), is not so as a modest variation of the surface proportion of low-coordination metal sites is expected for particle sizes in the range of $d(Co^0)$ = 5.6–10.4 nm. This is clearly perceived in Fig. S2 (Supplementary material) where the surface proportion of corner sites is plotted against $d(Co^0)$ for a cuboctahedral model cobalt nanoparticle [56]. In contrast, marked variations in the proportion of defect sites with $d(Co^0)$ are expected for sizes below 4 nm, where the classical structure sensitivity manifests [23]. Finally, a high-frequency shoulder at 2060 cm^{-1} is observed for 10%Co/ITQ(4) (Fig. 8b). The assignment of the 2060 cm^{-1} IR band is quite controversial in the literature and dicarbonyl species attached to cobalt defect sites [29], a partially hydrogenated Co(H)-CO structure [57], and CO adsorbed on $Co^{\delta+}$ sites have been considered [58–60]. The assignment to dicarbonyl species is not consistent with our results as it would require the existence of coupled bands for the symmetric and antisymmetric vibration modes and which are not detected in our spectra. Additionally, the possible assignment of the 2060 cm^{-1} band to a partially hydrogenated Co(H)CO adsorbed species is neither pertinent as the high temperature evacuation performed after the *in situ* catalyst reduction ensures an efficient removal of adsorbed H_2 [37,61]. We thus tentatively ascribe the 2060 cm^{-1} shoulder appearing in the spectrum of as-reduced 10%Co/ITQ(4) to CO adsorbed on interface cobalt sites in close contact with the support. The presence of oxygen at the support surface would induce a more electropositive character on these adjacent cobalt sites ($Co^{\delta+}$). This assignment is in concordance with the expected higher Co-support contact surface for the 10%Co/ITQ(4) catalyst displaying the smallest particle size. A careful examination of previously reported CO-FTIR results on cobalt catalysts shows that other authors have also found an enhanced adsorption band at 2060–2070 cm^{-1} when decreasing the mean cobalt particle size in Co/Al_2O_3 [57,62] and (*fcc*)Ru–Co/SBA-15 [63] catalysts. Additionally, no FTIR bands at ca. 2175 cm^{-1} related to CO adsorbed on Co^{2+} sites (cobalt oxide or silicates) have been found in these three reduced catalysts, which further supports the high extent of reduction achieved, already inferred from the H_2-TPR results. An adsorption band at this frequency is observed, by contrast, in the CO-FTIR spectrum of a partially reduced catalyst, such as 10%Co/ITQ(5), under the same experimental conditions (not shown).

The spectra evolution has been studied also by progressively increasing the CO dosage in the FTIR cell at RT. Marked and similar variations in the spectra have been found for 10%Co/ITQ(1) and 10%Co/ITQ(4) model catalysts upon increasing CO dosage. As representative for these two catalysts, Fig. 9 shows the FTIR spectra of 10%Co/ITQ(1) for CO pressures of 5–250 mbar (the corresponding spectra for 10%Co/ITQ(4) has been included in the Supplementary material as Fig. S3). New intense bands at 2024 and 2002 cm^{-1} develop when the CO pressure increases. The lower frequency and higher stability (upon evacuation) of the 2024 and 2002 cm^{-1} IR bands versus the 2050 cm^{-1} band suggest adsorption on lower coordinated cobalt surface sites. Interestingly, re-adsorption of CO on the Co/ITQ-2 catalysts after evacuation does not reproduce the original spectra (P_{CO} = 5 mbar) as it is shown in the inset of Fig. 9 for 10%Co/ITQ(1). A similar behaviour is manifested by 10%Co/ITQ(4). The unrepeatable IR spectra points towards Co surface reconstruction on the metallic particles when the CO pressure is increased, which appears irreversible upon evacuation at RT. A completely different behaviour is observed in Fig. 10 on sample 10%Co/SiO_2 for which no new bands appear at increasing CO pressure. Moreover, after re-adsorption of CO on the evacuated 10%Co/SiO_2 sample, the initial spectra are completely recovered (shown in inset of Fig. 10 for P_{CO} = 5 mbar). Thus, no reconstruction of the cobalt surface can be inferred in this case. The CO-induced Co surface reconstruction has been previously proposed on the basis of STEM [28] and PM-RAIRS [29] results on monocrystalline cobalt foils heated in the presence of CO or syngas. Our results suggest that this surface reconstruction might take place for small supported Co nanoparticles at RT and in the absence of H_2. It seems, besides, that the reconstruction of the cobalt surface is somehow size dependent, being more favourable on relatively small cobalt nanoparticles, as those present in the micelle-synthesised Co/ITQ-2 model catalysts, and less favourable on largest particles, as those present in 10%Co/SiO_2.

Additionally, a detailed inspection of the FTIR spectra in the low frequency range (700–300 cm^{-1}) evidences that new bands, mainly at 642, 612 and 573 cm^{-1} develop upon increasing the CO dosage (5–250 mbar) on samples 10%Co/ITQ(1) and 10%Co/ITQ(4), as shown in Figs. 9 and S2. These low-frequency bands are, by contrast, absent on sample 10%Co/SiO_2 (Fig. 10). Metal–carbon and metal–oxygen stretching vibration modes are known to

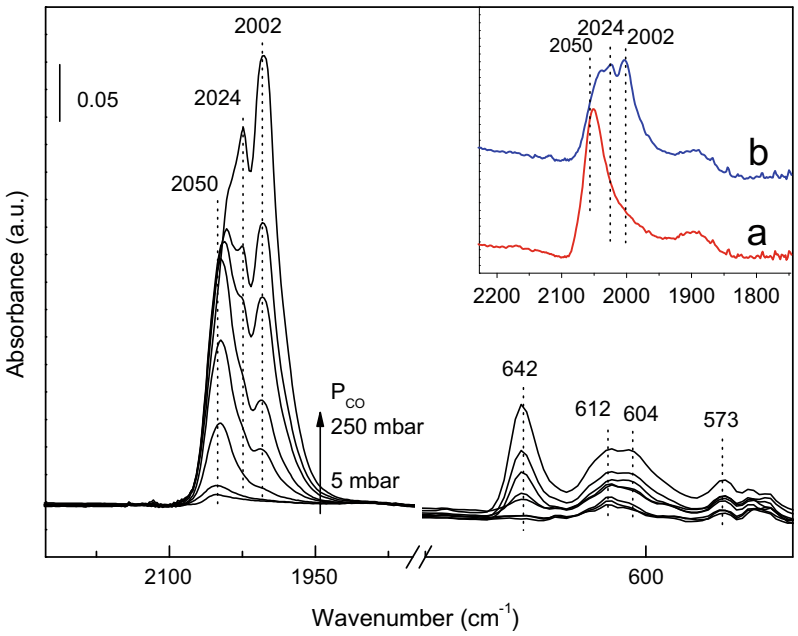

Fig. 9. Evolution of the CO-FTIR spectra with increasing CO dosages (P_{CO} = 5–250 mbar) on the pre-reduced 10%Co/ITQ(1) catalyst. The inset shows the spectra in the Co–carbonyl region at low coverage (P_{CO} = 5 mbar) for (a) the as-reduced sample and (b) after high CO dosage (P_{CO} = 250 mbar) and subsequent evacuation.

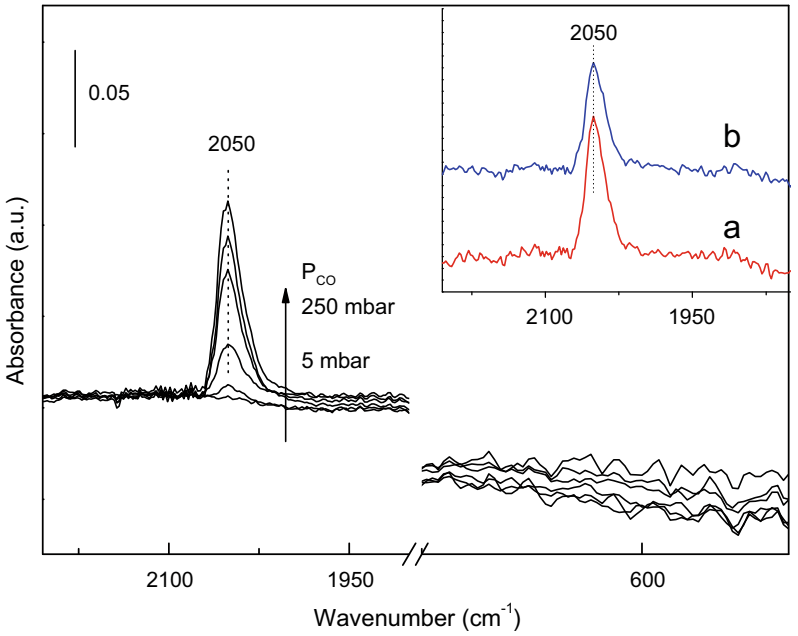

Fig. 10. Evolution of the CO-FTIR spectra with CO dosages (P_{CO} = 5–250 mbar) on the pre-reduced 10%Co/SiO_2 catalyst. The inset shows the spectra in the Co–carbonyl region at low coverage (P_{CO} = 5 mbar) for (a) the as-reduced sample and (b) after high CO dosage (P_{CO} = 250 mbar) and subsequent evacuation.

appear in this low IR frequency region (700–300 cm^{-1}). Indeed, the Co–O stretching mode has been reported at 612 cm^{-1} [64]. Moreover, the Co–C stretching mode of Co–CH_3 groups has been reported at 522 cm^{-1} [65], while bands at 560 and 643 cm^{-1} have been assigned by Lavrentiev et al. [66] to cobalt carbide species. Thus, dissociation of CO on cobalt surface sites leading to the adsorption of O and C adatoms can be inferred from the emergence of the bands at 612 cm^{-1} (Co–O) and 573 and 642 cm^{-1} (which we ascribe to surface Co–C species). Interestingly, according to our results, the development of these low-frequency bands seems to be linked to the development of the carbonyl bands at 2024 and 2002 cm^{-1} ascribed to more open crystallographic cobalt planes, or defect sites, as a consequence of the surface reconstruction. Therefore a cobalt surface reconstruction due to adsorbed O or C adatoms can be inferred. Indeed, while most authors had assumed cobalt sub-carbonyls ($Co(CO)_x$) as responsible for the cobalt surface reconstruction [28,29,67,68], very recent theoretical DFT results point to the determinant role of adsorbed carbon adatoms as responsible for surface *clock*-reconstruction on *fcc* Co^0 crystal facets [30]. The fact that only particles of size less than ca. 11 nm suffer from reconstruction at RT, in the absence of H_2, points to the decisive role of defect sites present, although in low amount,

on the small cobalt nanoparticles in 10%Co/ITQ(1) and 10%Co/ITQ(4) (band at ca. 2010 cm^{-1} in Fig. 8). Despite their low total proportion, as expected from the particle sizes >5 nm (see Fig. S2), these coordinatively unsaturated Co^0 sites should have a lower energy barrier to dissociate CO due to an enhanced metal-to-CO electron back-donation, as corroborated by many recent theoretical calculations on model clusters [24,25], and thus might behave as a source of dissociated CO (C and O adatoms) which may be spilled over the nearby planar sites (identified by the original carbonyl band at 2050 cm^{-1}) promoting surface reconstruction.

3.5.2. Site evolution during FTS at atmospheric pressure

The evolution of the Co catalysts *at work* in the Fischer–Tropsch reaction has also been monitored by CO-FTIR experiments using "freshly" reduced catalysts under flowing syngas. IR spectra at increasing temperature (298–493 K) have been collected. Since the three studied samples display similar trends, Fig. 11 shows only the spectra for 10%Co/ITQ(1), as representative. At 298 K two main bands, one at 2048 cm^{-1} associated to CO linearly adsorbed on *fcc* Co^0, and another one at 1625 cm^{-1} due to deformation modes for adsorbed water, probably deposited on the support from traces in the reactant feed, are observed. The presence of co-adsorbed H_2 or the lower contact time in flow conditions appears to avoid the surface reconstruction at RT in this case, as bands in 2024 and 2002 cm^{-1} are not clearly developed. Upon increasing the temperature to 433 K and 473 K, the band at 1625 cm^{-1} due to water is the main one observed in the 1500–2100 cm^{-1} region. The absence of bands for Co carbonyls in the region of 2000–2060 cm^{-1} might be due to a complete blockage of the surface sites due to activated H, CH_x or O adsorbed species. The presence of adsorbed oxygen species can indeed be inferred from the band at 612 cm^{-1}, the unique appearing in the low-frequency range (300–700 cm^{-1}). After increasing the temperature up to 493 K (applied also for the FTS catalytic experiments) time-resolved spectra are collected in Fig. 11. This reaction temperature rapidly restores the Co–carbonyl bands, likely due to desorption of reaction intermediates leaving free metal sites available for CO adsorption. Interestingly, the evolution of the IR spectra in the region of Co–carbonyls (1800–2080 cm^{-1}) under FTS for all the studied catalysts, including the low-dispersed 10%Co/SiO_2, is similar to that observed at *RT* and high pure CO dosages (Fig. 9), in that case restricted to rather small Co nanoparticles on 10%Co/ITQ(1) and 10%Co/ITQ(4). This fact reveals a similar surface reconstruction during FTS as that found at *RT* under pure CO. Simultaneously, the band due to water is enhanced due to its formation as a reaction product while a new band at 1591(sh) cm^{-1} associated to C–C stretching modes appears as an evidence of chain-growing processes occurring during the FTS. The relative intensity of the latter is substantially higher on sample 10%Co/ITQ(1) than on samples 10%Co/ITQ(4) and 10%Co/SiO_2 in agreement with the higher Co-time-yield observed for this sample in the high pressure FTS experiments (Table 5). Thus, taking into account the pressure gap and other hydrodynamic differences between the IR and the macro reactor experiments, *at work* CO-FTIR experiments are qualitatively representative of the catalytic behaviour of the samples under FTS, confirming the lower value of TOF for Co nanoparticles of size 5.6 nm than for particles larger than 10 nm. Additionally, it is very interesting how in Fig. 11 the IR band at 642 cm^{-1}, ascribed to surface carbidic species (adsorbed C adatoms) again developes strictly simultaneous to the IR bands at 2024 and 2002 cm^{-1}. In agreement with recent results based on theoretical calculations [30], these experiments provide the first conclusive experimental evidence, to the best of our knowledge, for the key role of carbidic carbon as the Co surface reconstruction agent in the FTS. Very recently, similar evidences have been reported on the formation of *true-active-sites* created by metal restructuring due to the incorporation of C adatoms, derived from the dissociation of the very early adsorbed reactant molecules, inside the outermost metallic layers of the catalytic Pd nanoparticles during alkyne hydrogenation reactions [69,70]. The fact that, unlike under pure CO at *RT*, the 10%Co/SiO_2 also suffers from surface reconstruction under FTS conditions, suggests a key role of H_2 (and/or temperature) in promoting CO dissociation on planar sites and the consequent surface reconstruction. Indeed, a H_2-assisted CO dissociation, through partially hydrogenated $(H)_xCO$ species as intermediates, has been lately suggested by DFT calculations on model Ni and Co surfaces [71,72]. The presence of co-activated hydrogen, and the assumption of a pre-hydrogenated $(H)_xCO$ species was shown to lower the energy

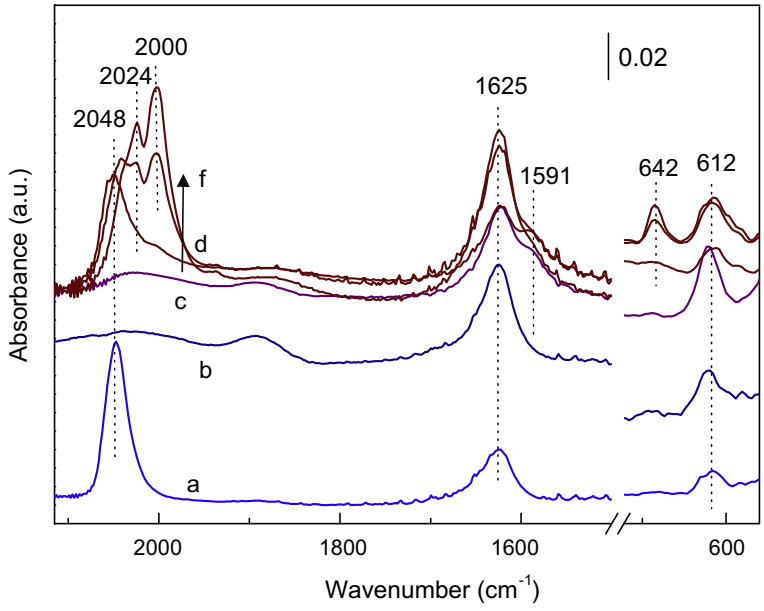

Fig. 11. Temperature-resolved IR spectra for the pre-reduced 10%Co/ITQ(1) catalyst under syngas flow at (a) *RT* (b) 433 K, (c) 473 K; and time-resolved IR spectra of the catalyst under FTS conditions (T = 493 K, P_{atm}) after (d) 120, (e) 210 and (f) 240 min on-stream.

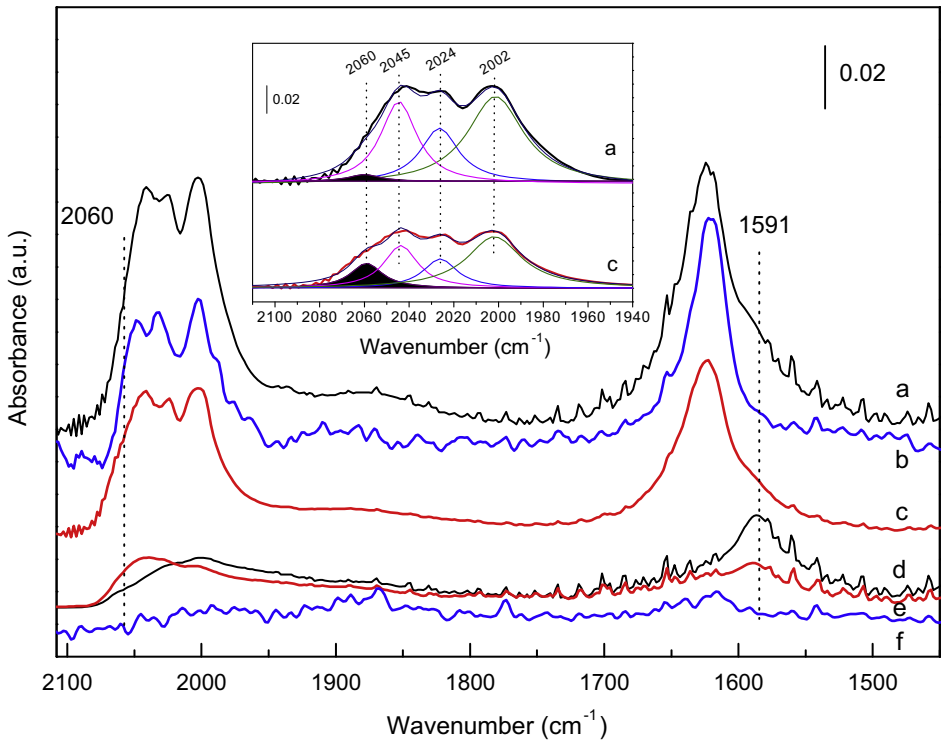

Fig. 12. FTIR spectra after 4 h on-stream in FTS (T = 493 K, P_{atm}) for (a) 10%Co/ITQ(1), (b) 10%Co/SiO_2 and (c) 10%Co/ITQ(4) model catalysts; and evacuation spectra at 298 K after FTS for (d) 10%Co/ITQ(1), (e) 10%Co/ITQ(4) and (f) 10%Co/SiO_2 model catalysts.

barrier for CO dissociation on flat sites approaching it to the more favourable dissociation on defect sites [71,72]. Summarising, the results suggest that the nature and extent of cobalt surface reconstruction during FTS seems to be similar on all samples, and thus particle size independent.

Despite the similar nature of surface reconstruction irrespective of the Co particle size suggested by the above results, some differences arise from the *at work* CO-FTIR study. Fig. 12 (spectra a, b, c) shows the IR spectra obtained at 493 K after 4 h on-stream for the three studied catalysts. In addition to cobalt carbonyl species (IR bands at 2050–1900 cm^{-1}), water (1625 cm^{-1}) and surface C_{2+} species (1591 cm^{-1}, as a very weak shoulder for those samples displaying lower cobalt-time-yields), which are observed for all the samples, the 2060 cm^{-1} contribution in the spectrum for 10%Co/ITQ(4) is clearly perceptible. This band, already present as a weak shoulder in the spectrum for the as-reduced sample (Fig. 8), has been enhanced during the relatively short TOS (4 h) under ambient-pressure FTS. This is clearly evidenced in the inset of Fig. 12 showing a detailed view and Lorentzian curve-fitting in comparison to the 10%Co/ITQ(1), for which the band at 2060 cm^{-1} cannot be clearly perceived even after reaction. Moreover, at the evacuated spectra (Fig. 12, spectra d, e, f) the higher contribution of this IR band at 2060 cm^{-1} for 10%Co/ITQ(4) with respect to the bands at 2050–2000 cm^{-1} which are prominent for 10%Co/ITQ(1) can be observed. Worth to be mentioned is that a high temperature (723 K) evacuation (10^{-5} bar) treatment, required to remove any adsorbed species of the catalysts, depletes the low-frequency bands (700–300 cm^{-1}), restores the original band at 2050 cm^{-1} as the unique carbonyl signal and lowers the contribution at 2060 cm^{-1} for 10%Co/ITQ(4) (spectra not shown), pointing to the instability of the restructuring carbidic species upon evacuation and to the reversibility of the surface reconstruction at high temperatures and encouraging *operando* characterisation to gain valuable information on this catalytic system. It seems, thus, that the proportion of interfacial $Co^{\delta+}$ sites significantly augments, once the FTS is activated, for the catalyst having the smallest particle size (5.6 nm). On the contrary, a noticeable contribution at 2060 cm^{-1} cannot be unambiguously discerned in the CO-FITR spectra for the catalysts displaying $d(Co^0) > 10$ nm. They are equally remarkable both that there are not significant differences in the CO-FTIR spectra during catalysis for 10%Co/ITQ(1) and 10%Co/SiO_2 catalysts, whose particle size differ one order of magnitude, and that the contribution at 2060 cm^{-1} is the only found spectral difference between the former samples (displaying the same TOF) and 10%Co/ITQ(4), which shows a 7-fold lower intrinsic site-activity in FTS at 2.0 MPa (Table 5). Besides, no bands at 2175 cm^{-1} (CO–Co^{2+}) are observed after 4 h on-stream which discards, at the sensibility level of the technique, a significant re-oxidation of the catalysts.

We ascribe the lower catalytic TOF observed for the very small nanoparticles to the higher proportion of the electropositive Co-support interfacial sites that are expected to display a lower intrinsic activity for CO dissociation [50]. The contribution of these sites becomes negligible for $d(Co^0) > 10$ nm where the TOF is constant up to $d(Co^0) \approx 150$ nm, according to our experimental results. It should be here mentioned that the Blyholder theory [50,54] predicts a lower absorption coefficient of CO adsorbed on these partially oxidised $Co^{\delta+}$ sites and thus their proportion might be underestimated by simply considering its contribution to the IR spectra (inset of Fig. 12). In addition, the relative population of $Co^{\delta+}$ sites might well be favoured at higher pressures and thus their contribution may be enhanced during the FTS experiments at 2.0 MPa, accounting for the 7-fold decrease in TOF found in the high-pressure catalytic experiments. As a matter of fact, the particle-size effect in TOF has been reported to be pressure dependent, occurring below 6 nm at 1 bar, but extending up to 8–9 nm at 35 bar [19].

The above results can be rationalised in terms of an enhanced contact between Co nanoparticles and support, probably as a result of a change in nanoparticle morphology, namely, flattening, which might be linked to the observed Co surface reconstruction. This

hypothesis is in agreement with the recently reported decrease in mean Co–Co coordination number ascertained by *at work*-EXAFS during atmospheric-pressure FTS for Co/CNF catalysts [19]. *Activated* CNFs display a rather high density of surface oxidic groups [73,74] which may allow to extend the present explanation also for that system, for which a similar non-classical particle size dependence for TOF has been already reported.

These changes in the particle shape are indeed apparent by TEM inspection of "spent" catalysts after 10 h on-stream under high-pressure FTS. Fig. 13 shows representative medium-resolution micrographs for the spent 10%Co/ITQ(2) catalyst. Dispersed cobalt nanoparticles are seen on the ITQ-2 nanosheets. Large agglomerates were not found, while some individual nanoparticles appear grouped as bunches. In this case, the passivation layer appears thinner (typically <1.5 nm) maybe because surface re-oxidation is hindered by adsorbed hydrocarbons. Besides, no apparent special morphology is perceived for those nanoparticles viewed from top, whose passivation-corrected mean particle size is estimated to be 10.3 nm, in contrast to the $d(Co^0)_T$ = 8.2 nm found for the original reduced-passivated sample. Nevertheless, those particles which are viewed in profile, i.e. those appearing at the support edge (arrows in Fig. 13), clearly display a raft-like shape, appearing as rods at the transmission observation, evidencing an enhanced surface-of-contact with the ITQ-2 support. The increase in $d(Co^0)_T$ for the spent catalyst with respect to the original as-reduced sample might well be a combination of a (limited) degree of metal sintering and the from-top observation of flattened nanoparticles.

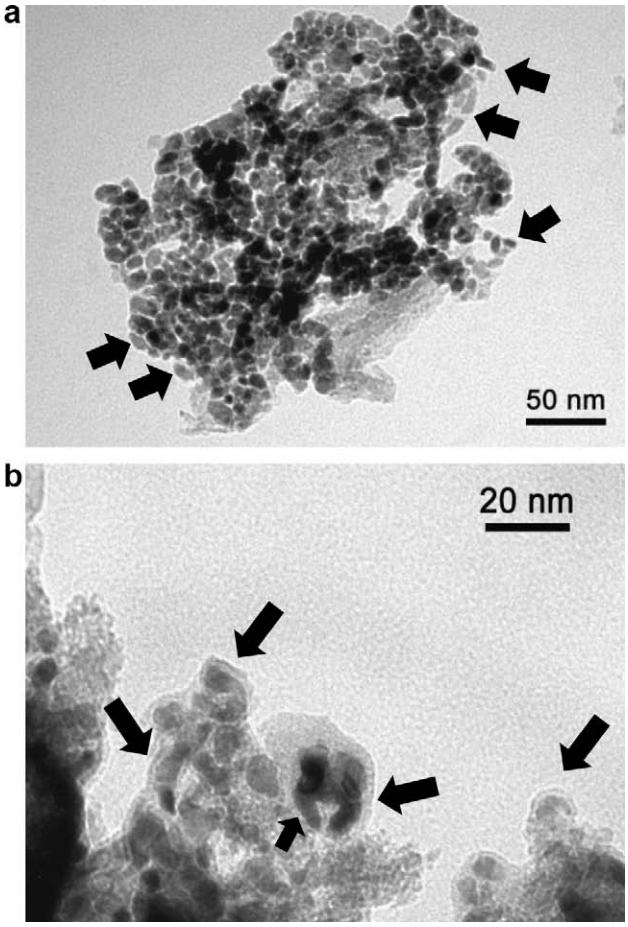

Fig. 13. (a) Representative TEM image for the spent 10%Co/ITQ(2) catalyst (after 10 h on-stream, T = 493 K, P = 2.0 MPa, X_{CO} = 10%) discarding extensive Co sintering and evidencing elongated raft-like Co nanoparticles (black arrows) viewed in profile at the support edges; and (b) detailed view at the support edge.

Dynamic (usually rapid and reversible) reactant-induced shape-changes have been lately addressed for other nanoparticulate catalysts thanks to *in situ* Environmental HRTEM (E-HRTEM) [75] and EXAFS [76]. Indeed E-HRTEM has proven that under (wet)H_2/CO flow a strong shape-change towards a disc-like morphology and an enhanced contact with the support takes place for the Cu/ZnO system employed in the hydrogenation of CO [75,77]. A similar flattening appears to take place for the Co/ITQ-2 catalysts under working conditions in the FTS, on the basis of our *at work* CO-FTIR study and the post-reaction *ex situ* characterisation. Beyond the novel picture presented in this work, the application of recent and on-going advances in characterisation techniques which allow for (nearly)environmental analysis [69,75,78] is expected to provide future in-depth insights on the UHV-unstable reconstructing Co–carbidic species and the particle morphology changes during reaction.

4. Conclusions

The combination of an *ex*-support reverse micellar synthesis, displaying varying microemulsion parameters, with a surface-silylated ITQ-2 delaminated zeolite as support allows to prepare 10%Co/ITQ-2 catalysts showing rather uniform metal particle sizes in the 5–11 nm range. This preparative methodology leads to highly reducible materials for $d(Co_3O_4) \geqslant 6.8$ nm, and allows us to conclude that the activation energies for the two Co_3O_4 reductive steps ($Co_3O_4 \rightarrow CoO \rightarrow Co^0$), are particle-size dependent. Further increasing metal dispersion promotes the progressive development of cobalt surface hydroxy-silicates and bulk silicates by reaction of the loaded metal against the silica support. When the FTS activity of the model Co/ITQ-2 catalysts is compared with that of a low-dispersed 30%Co/SiO_2 prepared by physically supporting Co_3O_4 nanopowder on commercial SiO_2, the TOF increases with $d(Co^0)$ in the 5.6–10.4 nm range and it remains rather constant up to $d(Co^0)$ = 141 nm, concurring with the non-classical particle size effect previously reported [19]. Additionally, CO-FTIR experimental evidences indicate that surface adsorbed C adatoms derived from CO dissociation are responsible for a cobalt surface reconstruction under ambient-pressure FTS conditions, and this surface reconstruction occurs similarly irrespective of the metal particle size in the 5.6–141 nm range. Moreover, the only spectroscopic difference between low and high TOF catalysts is the enhancement of partially oxidised interfacial $Co^{\delta+}$–SiO_2 sites for the smallest Co nanoparticles (5.6 nm) existing in the former, which appears to be a consequence of nanoparticle flattening under reaction conditions. As a step forward in understanding the non-classical particle size effect in Co-catalysed FTS, our results suggest that a higher relative concentration of these interfacial sites in flattened small Co nanoparticles is responsible for the decreased TOF observed for $d(Co^0)$ < 10 nm.

Acknowledgments

Financial support by the Comisión Interministerial de Ciencia y Tecnología (CICYT) of Spain through the Project CTQ2007-66614/PPQ is gratefully acknowledged. The authors thank Dr. J.L. Moya and M. Planes (Universidad Politécnica de Valencia) and Dr. S. Agouram (University of Valencia) for their assistance with TEM and HRTEM characterisation, M.T. Jimaré for aid with CO-FTIR experiments and R. Pérez for technical support on ITQ-2 preparation. G. Prieto thanks the Ministerio de Educación y Ciencia (MEC) of Spain for a FPU Ph.D. scholarship.

Appendix A. Supplementary material

Supplementary data associated with this article can be found, in the online version, at doi:10.1016/j.jcat.2009.06.001.

References

[1] M.E. Dry, Catal. Today 6 (1990) 183.
[2] I. Wender, Fuel Proc. Tech. 48 (1996) 189.
[3] E. Iglesia, Appl. Catal. A 161 (1997) 59.
[4] G.L. Bezemer, P.B. Radstake, V. Koot, A.J. van Dillen, J.W. Geus, K.P. de Jong, J. Catal. 237 (2006) 291.
[5] L. D'Souza, J.R. Regalbuto, J.T. Miller, J. Catal. 254 (2008) 157.
[6] K. Okabe, X. Li, M. Wei, H. Arakawa, Catal. Today 89 (2004) 431.
[7] J. Panpranot, J.G. Goodwin Jr., A. Sayari, Catal. Today 77 (2002) 269.
[8] A. Griboval-Constant, A.Y. Khodakov, R. Bechara, V.L. Zholobenko, J. Catal. 144 (2002) 609.
[9] A. Martínez, C. López, F. Márquez, I. Díaz, J. Catal. 220 (2003) 486.
[10] P. Concepción, C. López, A. Martínez, V.F. Puntes, J. Catal. 228 (2004) 321.
[11] L. D'Souza, L. Jiao, J.R. Regalbuto, J.T. Miller, A.J. Kropf, J. Catal. 248 (2007) 165.
[12] A. Martínez, G. Prieto, J. Rollán, J. Catal. 263 (2009) 292.
[13] J.R.A. Sietsma, J.D. Meeldijk, J.P. den Breejen, M. Versluijs-Helder, A.J. van Dillen, P.E. de Jongh, K.P. de Jong, Angew. Chem., Int. Ed. 46 (2007) 4547.
[14] A.Y. Khodakov, J. Lynch, D. Bazin, B. Rebours, N. Zanier, B. Moison, P. Chaumette, J. Catal. 168 (1997) 16.
[15] A.Y. Khodakov, A. Griboval-Constant, R. Bechara, V.L. Zholobenko, J. Catal. 206 (2002) 230.
[16] R.C. Reuel, C.H. Bartholomew, J. Catal. 85 (1984) 78.
[17] A.S. Lisitsyn, A.V. Golovin, V.L. Kuznetsov, Y.I. Yermakov, J. Catal. 95 (1985) 527.
[18] A. Barbier, A. Tuel, I. Arcon, A. Kodre, G.A. Martin, J. Catal. 200 (2001) 106.
[19] G.L. Bezemer, J.H. Bitter, H.P.C.E. Kuipers, H. Oosterbeek, J.E. Holewijn, X. Xu, F. Kapteijn, A.J. van Dillen, K.P. de Jong, J. Am. Chem. Soc. 128 (2006) 3956.
[20] I. Fernández-Morales, A. Guerrero-Ruiz, F.J. López-Garzón, I. Rodríguez-Ramos, C. Moreno-Castilla, Appl. Catal. 14 (1985) 159.
[21] E. Iglesia, S.L. Soled, R.A. Fiato, J. Catal. 137 (1992) 212.
[22] Ø. Borg, P.D.C. Dietzel, A.I. Spjelkavik, E.Z. Tveten, J.C. Walmsley, S. Diplas, S. Eri, A. Holmen, E. Rytter, J. Catal. 259 (2008) 161.
[23] M. Boudart, Chem. Rev. 95 (1995) 661.
[24] Q. Ge, M. Neurock, J. Phys. Chem. B 110 (2006) 15368.
[25] J. Cheng, X-Q. Gong, P. Hu, C.M. Lok, P. Ellis, S. French, J. Catal. 254 (2008) 285.
[26] E. van Steen, M. Claeys, M.E. Dry, J. van de Loosdrecht, E.L. Viljoen, J.L. Visagie, J. Phys. Chem. B 109 (2005) 3575.
[27] A.M. Saib, A. Borgna, J. van de Loosdrecht, P.J. van Berge, J.W. Geus, J.W. Niemantsverdriet, J. Catal. 239 (2006) 326.
[28] J. Wilson, C. de Groot, J. Phys. Chem. B 99 (1995) 7860.
[29] G.A. Beitel, C.P.M. de Groot, H. Oosterbeek, J.H. Wilson, J. Phys. Chem. B 101 (1997) 4035.
[30] I.M. Ciobîcă, R.A. van Santen, P.J. van Berge, J. van de Loosdrecht, Surf. Sci. 602 (2008) 17.
[31] A. Martínez, G. Prieto, J. Catal. 245 (2007) 470.
[32] A. Corma, V. Fornés, S.B. Pergher, Th.L.M. Maesen, J.G. Buglass, Nature 396 (1998) 353.
[33] A. Martínez, G. Prieto, Catal. Commun. 8 (2007) 1479.
[34] C.P. Gibson, K.J. Putzer, Science 267 (1995) 1338.
[35] Z. Gui, R. Fan, W. Mo, X. Chen, L. Yang, Y. Hu, Mater. Res. Bull. 38 (2003) 169.
[36] D. Schanke, S. Vada, E.A. Blekkan, A.M. Hilmen, A. Hoff, A. Holmen, J. Catal. 156 (1995) 85.
[37] R.C. Reuel, C.H. Bartholomew, J. Catal. 85 (1984) 63.
[38] D.-H. Chen, S.-H. Wu, Chem. Mater. 12 (2000) 1354.
[39] T. He, D. Chen, X. Jiao, Y. Wang, Y. Duan, Chem. Mater. 17 (2005) 4023.
[40] Y. Okamoto, K. Nagata, T. Adachi, T. Imanaka, K. Inamura, T. Takyu, J. Phys. Chem. 95 (1991) 310.
[41] A.A. Verberckmoes, B.M. Weckhuysen, R.A. Schoonheydt, Micropor. Mesopor. Mater. 22 (1998) 165.
[42] E. van Steen, G.S. Sewell, R.A. Makhothe, C. Micklethwaite, H. Manstein, M. de Lange, C.T. O'Connor, J. Catal. 162 (1996) 220.
[43] S. Krishnamoorthy, M. Tu, M.P. Ojeda, D. Pinna, E. Iglesia, J. Catal. 211 (2002) 422.
[44] A.M. Saib, A. Borgna, J. van de Loosdrecht, P.J. van Berge, J.W. Niemantsverdriet, Appl. Catal. A 312 (2006) 12.
[45] R. Van Hardeveld, F. Hartog, Surf. Sci. 15 (1969) 189.
[46] J.N. Kuhn, W. Huang, C-K. Tsung, Y. Zhang, G.A. Somorjai, J. Am. Chem. Soc. 130 (2008) 14026.
[47] F. Hoxha, N. van Vegten, A. Urakawa, F. Krumeich, T. Mallat, A. Baiker, J. Catal. 261 (2009) 224.
[48] A. Martínez, G. Prieto, R. Murciano, Abstract of the 21st North American Meeting, North American Catalysis Society (NAM-NACS), San Francisco, USA, June 7–11, 2009.
[49] E. Iglesia, S.C. Reyes, R.J. Madon, J. Catal. 129 (1991) 238.
[50] G. Blyholder, J. Phys. Chem. 68 (1964) 2772.
[51] S. Sun, N. Tsubaki, K. Fujimoto, Appl. Catal. A 202 (2000) 121.
[52] J.L. Zhang, J.G. Chen, J. Ren, Y.H. Sun, Appl. Catal. A 243 (2001) 59.
[53] D. Song, J. Li, Q. Cai, J. Phys. Chem. C 111 (2007) 18970.
[54] G. Blyholder, L.D. Neff, J. Phys. Chem. 73 (1969) 3494.
[55] L.E.S. Rygh, C.J. Nielsen, J. Catal. 194 (2000) 401.
[56] R.E. Benfield, J. Chem. Soc. Faraday Trans. 88 (1992) 1107.
[57] M.J. Heal, E.C. Leisegang, R.G. Torington, J. Catal. 51 (1978) 314.
[58] J.G. Choi, H.K. Rhee, S.H. Moon, Appl. Catal. 13 (1985) 269.
[59] G. Kadinov, Ch. Bonev, S. Todorova, A. Palazov, J. Chem. Soc. Faraday Trans. 94 (1998) 3027.
[60] L.E.S. Rygh, O.H. Ellestad, P. Klæboe, C.J. Nielsen, Phys. Chem. Chem. Phys. 2 (2000) 1835.
[61] R.D. Jones, C.H. Bartholomew, Appl. Catal. 39 (1988) 77.
[62] V.B. Kazanskii, A.V. Zaitsev, V.Y. Borokov, A.L. Lapidus, Appl. Catal. 40 (1988) 17.
[63] H. Xiong, Y. Zhang, K. Liew, J. Li, J. Mol. Catal. A 295 (2008) 68.
[64] Z. Hu, L. Mo, X. Feng, J. Shi, Y. Wang, Y. Xie, Mater. Chem. Phys. 114 (2009) 53.
[65] S. Nie, L.G. Marzilli, N.T. Yu, J. Am. Chem. Soc. 111 (1989) 9256.
[66] V. Lavrentiev, H. Abe, S. Yamamoto, H. Naramoto, K. Narumi, Surf. Interf. Anal. 35 (2003) 36.
[67] G.A. Beitel, A. Laskov, H. Oosterbeek, E.W. Kuipers, J. Phys. Chem. B 100 (1996) 12494.
[68] N. Kruse, J. Schweicher, A. Bundhoo, A. Frennet, T. Visart de Bocarmé, Top. Catal. 48 (2008) 145.
[69] D. Teschner, J. Borsodi, A. Wootsch, Z. Révay, M. Hävecker, A. Knop-Gericke, S.D. Jackson, R. Schlögl, Science 320 (2008) 86.
[70] D. Teschner, Z. Révay, J. Borsodi, M. Hävecker, A. Knop-Gericke, R. Schlögl, D. Miltroy, S.D. Jackson, D. Torres, P. Sauet, Angew. Chem., Int. Ed. 47 (2008) 1.
[71] M.P. Andersson, F. Abild-Pedersen, I.N. Remediakis, T. Bligaard, G. Jones, J. Engbæk, O. Lytken, S. Horch, J.H. Nielsen, J. Sehested, J.R. Rostrup-Nielsen, J.K. Nørskov, I. Chorkendorff, J. Catal. 255 (2008) 6.
[72] O.R. Inderwildi, S.J. Jenkins, D.A. King, J. Phys. Chem. C 112 (2008) 1305.
[73] M.L. Toebes, J.M.P. Heeswijk, J.H. Bitter, A.J. van Dillen, K.P. de Jong, Carbon 42 (2004) 307.
[74] Z. Yu, Ø. Borg, D. Chen, E. Rytter, A. Holmen, Top. Catal. 45 (2007) 69.
[75] P.L. Hansen, J.B. Wagner, S. Helveg, J.R. Rostrup-Nielsen, B.S. Clausen, H. Topsøe, Science 295 (2002) 2053.
[76] M.A. Newton, C. Belver-Coldeira, A. Martínez-Arias, M. Fernández-García, Nature 6 (2007) 528.
[77] P.C.K. Vesborg, I. Chorkendorff, I. Knudsen, O. Balmes, J. Nerlov, A.M. Molenbroek, B.S. Clausen, S. Helveg, J. Catal. 262 (2009) 65.
[78] E. de Smit, I. Swart, J.F. Creemer, G.H. Hoveling, M.K. Gilles, T. Tyliszczak, P.J. Kooyman, H.W. Zandbergen, C. Morin, B.M. Weckhuysen, F.M.F. de Groot, Nature 456 (2008) 222.